ABSTRACT

Title of Document: SUPER RESOLUTION IMAGING AND NANOSCALE MAGNETIC DETECTION IN MICROFLUDIC DEVICE.

Kangmook Lim, Ph.D., 2015

Directed By: Professor. Edo Waks
Department of Electrical and Computer Engineering

Nanoscale sensing and imaging tools are the most emerging techniques in fields of nanoscience research and engineering. To demonstrate nanoscale sensing and imaging tools, it is required to achieve high sensitivity and spatial resolution simultaneously. By fulfilling the requirements, this thesis describes mainly two different scanning applications employing quantum probes and nanoparticle positioning technique using fluid flow control.

First, we develop a method that can systematically probe the distortion of an emitter's diffraction spot near a nanoparticle in a microfluidic device. The results provide a better fundamental understanding of near-field coupling between emitters and nanophotonic structures. We demonstrate that by monitoring the distortion of the diffraction spot we can perform highly accurate imaging of the nanoparticle with 8 nm spatial precision.

Next, we develop a method to perform localized magnetometry in a microfluidic device with a 48 nm spatial precision. We map out the local field distribution of a magnetic nanoparticle by manipulating it in the vicinity of an immobilized single NV center and optically detecting the induced Zeeman shift with a magnetic field sensitivity of 17.5 $\mu T\ Hz^{-1/2}$.

Finally, we introduce a scanning magnetic field technique that employs multiple NV centers in diamond nanocrystals suspended in microfluidic channels. This technique has advantages of short acquisition time over wide-field with nanoscale spatial resolution. The advantages make our technique attractive to a wide range of magnetic imaging applications in fluidic environments and biophysical systems.

SUPER RESOLUTION IMAGING AND NANOSCALE MAGNETIC DETECTION IN MICROFLUDIC DEVICE.

By

Kangmook Lim

Dissertation submitted to the Faculty of the Graduate School of the
University of Maryland, College Park, in partial fulfillment
of the requirements for the degree of
Doctor of Philosophy
2015

Advisory Committee:
Professor Edo Waks, Chair
Professor Christopher Davis
Professor Thomas Murphy
Professor Jeremy Munday
Professor Benjamin Shapiro

Acknowledgements

First of all, I am incredibly grateful to my advisor, Prof. Edo Waks, for his support, guidance and encouragement throughout my doctoral work. He has inspired me with his tremendous scientific interest, extraordinary enthusiasm on the research projects and great insights into the problems.

I am very grateful to Prof. Benjamin Shapiro for collaboration and discussions on the microfluidics. My research projects and this thesis would not have been possible without his support. I would also like to thank my other thesis committee members Prof. Christopher Davis, Prof. Thomas Murphy and Prof. Jeremy Munday for their valuable guidance and comments on my thesis projects.

I would also like to acknowledge all my labmates Dr. Deepak Sridharan, Dr. Chad Ropp, Dr. Shilpi Gupta, Dr. Ranojoy Bose, Dr. Hyochul Kim, Thomas Shen, Shuo Sun, Tao Cai, Dr. Kaushik Roy, Zhili Yang and Dr. Jehyung Kim for their help and support and for being such great colleagues and friends.

Finally, I would like to thank my family for their unlimited love and support. I could not have done any of it without their belief in me.

Table of Contents

List of Figures

Chapter 1: Introduction

1.1 Motivation

Nanoparticles possess unique properties allowing for use in a wide range of applications from science to engineering. For examples, metal nanoparticles have been used in bioimaging [1-3], chemical reactions [4, 5] and plasmonics [6-8]. The reaction of magnetic nanoparticles to a magnetic force has been utilized in applications such as drug delivery [9, 10], cell sorting [11, 12] and magnetic resonance imaging [10, 13]. To study and utilize the nanoparticles, it is required to develop nanoscale sensing and imaging techniques. To probe the nanoparticles with high spatial resolution, the size of sensors is demanded in nanoscale. Quantum probes are ideal platforms for the nanoparticles due to their size. To take advantage of the quantum probes, nanoparticle positioning techniques are required that can position the interesting nanoparticle to the quantum probe with nanoscale precision. Optically tracking the quantum probe and the nanoparticle allows us to explore nanoscale physics. In this chapter, I discuss the super-resolution microscopy which is able to image the nanoparticles with nanoscale resolution, the nanoparticle positioning technique using fluid flow control and the nitrogen-vacancy color center in diamond crystals.

1.2 Super-resolution microscopy

Optical microscopy allows to observe objects that are smaller than we can see with simple operation and low expense. Due to the advantages, the optical microscope has become an essential tool to study chemistry, biology and materials science. The spatial resolution of the microscope, however, has reached a fundamental limit due to the optical diffraction effect [14]. The minimum feature size which can be resolved with the microscope is

$$d = \frac{\lambda}{2n \sin \Theta} \quad (1)$$

, where λ is the wavelength of light and $n \sin \Theta$ is the numerical aperture (NA) of the objective lens. Base on the experiment setup used in this thesis, for example, the theoretical resolution is expected as good as 214 nm with λ of 620 nm and NA of 1.45. As scientists have focused on extremely small objects such as cells, molecules and nanoparticles, this optical diffraction limit has remained to be developed for many years.

Super-resolution optical microscopy has emerged as a technique to overcome the diffraction limit of light and provide imaging resolution better than 10 nm [15-20]. The super-resolution techniques utilize tiny isolated emitters (e.g., quantum dots and dyes) placed at or near the object surface. The fluorescent emission will be formed a diffraction-limited spot and projected onto the CCD over multiple pixels [21]. To

localize the emitter position, the diffraction-limited images are analyzed by fitting to a two-dimensional Gaussian function. This approach allows us to track the centroid position of the individual emitter much better than diffraction limit based on the collected photon numbers, the width of diffraction-limited spot, the pixel size and the background noise [21, 22]. By repeating the process over many cycles, we can construct a high-resolution optical image of the nanoscale object by plotting all of the centroid positions.

This technique has emerged as a versatile approach for attaining sub-wavelength information in a broad range of applications in biology [23-26] and chemistry [5, 27-29]. More recently, a number of works have applied super-resolution imaging techniques to probe photonic nanostructures such as metallic hot spots [22, 30, 31], nanowires [32, 33], nanoparticles [34, 35] and nanoantennas [36, 37]. These techniques have imaged the local density of states of nanostructures with reported spatial precision that is finer than 50 nm [33, 38]. In nanophotonic systems, the centroid positions are less correlated to the actual position of the emitter due to the near-field coupling between the dipole emission and the nanostructure, and will be discussed in more detail in the chapter 2.

1.3 Microfluidic nanoparticle positioning

1.3.1 Overview

The ability to control position of individual nanoparticles at the nanoscale is of substantial interest in nanoscience. Such a technique is essential for a broad range of applications in the fields of nanofabrications [39], electronics [40], photonics [41, 42], quantum information [43, 44] and biology [45]. In particular, combining a nanoscale manipulation technique with a quantum probe could enable to build nanoscale sensing and imaging systems which is emerging field of nanoengineering. To accomplish nanoscale positioning, wide verity approaches have been developed and improved. These approaches fall into mainly two categories depending on the requirement of physical contacts to the nanoparticles.

In the positioning techniques involving physical contact, sharp mechanical tips are used to pick and place nanoparticles [46]. These techniques generally provide high resolution AFM images using the same mechanical tip to position the nanoparticles [47]. However, the mechanical tips require appropriate chemical electrical properties to interact with the nanoparticles and provide limited reproducibility of positioning. Moreover, the mechanical contacts can change the properties of the nanoparticles or damage the nanoparticles during the positioning [48].

Optical tweezers use optical gradient forces of a laser to manipulate objects without physical contacts [49, 50]. Those optical gradient forces make possible to trap an object in the three-dimensional potential, rotate the trapped object along the polarization and move it by translating the trap laser. However, the required trapping force depends on the volume of the object [51]. As a result, trapping nanoparticles are challenging due to the small size. The optical gradient force is exerted to the all the nanoparticles in the laser beam and aggregate them at the center of the beam. For nanophotonic applications, the trapping laser can complicate the optical measurements. Furthermore, the trapping laser can locally heat up the sample, resulting in unwanted chemical interactions and damages to biological samples [52].

1.3.2 Fluid flow positioning

In this thesis, electroosmotic flow technique is adapted to control individual nanoparticles suspended in a microfluidic channel [53]. Figure 1 illustrates operation principle of the fluid flow positioning. In microfluidic channel, an electric field induced by electrods actuates a layer of ions at the surface of the channel. The ion motion flows the fluid in the microfluidic channel. This mechanism moves any particles suspended in the microfluidic channel along with the surrounding fluid.

The key advantage of fluid flow techniques is that the manipulation is possible without damages to the nanoparticles, since it is the background fluid which drags the nanoparticles. With this technique, manipulation of a variety of nanoparticles is

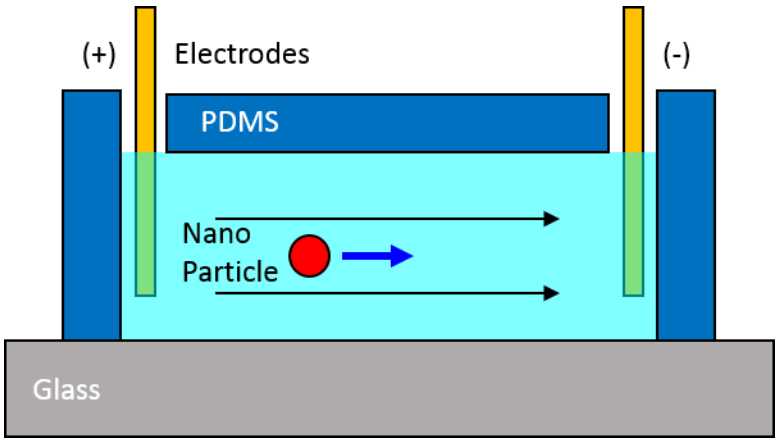

Figure 1: Illustration of operation principle of the fluid flow positioning. Electroosmotic flow moves any particles suspended in the fluid.

feasible regardless of size and material of the nanoparticles. A fluid chemistry has been engineered to play an important role in the positioning. By adding rheology modifier to the fluid, the viscosity of the fluid is increased to reduce the diffusion motion of the nanoparticles [54]. A water-soluble multifunctional acrylic monomer makes the nanoparticles confined at the surface of the microfluidic channel [55]. Consequently, the fluid flow techniques effectively manipulate the nanoparticles along the surface of the microfluidic channel.

Two-dimensional positioning is available with a cross shape microfluidic channel [56]. Figure 2 illustrates that a nanoparticle is being positioned in the control area of the cross microfluidic channel. There are four electrodes at the end of each channel, applying electric fields to the microfluidic channel in four different directions. Composing different combinations of the four actuation directions, the microfluidic device can position the nanoparticle toward any direction.

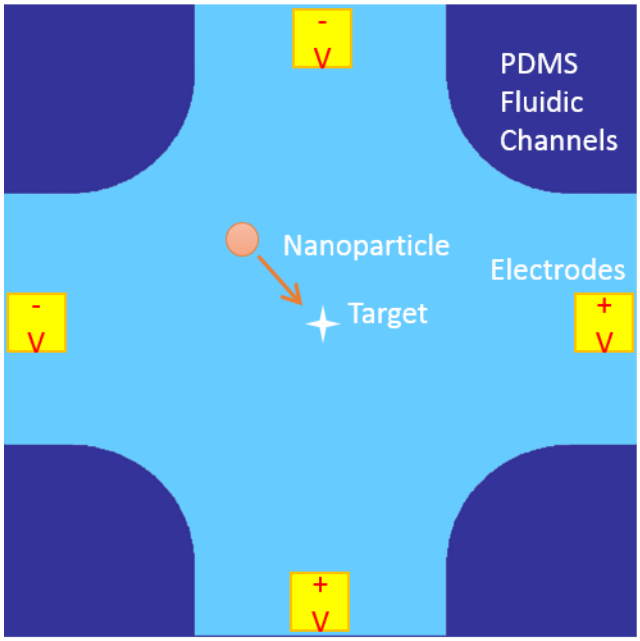

Figure 2: Schematic of microfluidic device for 2D control of nanoparticles. The cross shape microfluidic channel enables 2D positioning of the nanoparticles using four electrodes.

1.3.3 Active feedback positioning

In order to achieve active positioning of the nanoparticles, the fluid flow positioning techniques combine with a vision-based feedback control system as illustrated in Figure 3. The image of interesting nanoparticle is projected onto a CCD camera using a microscope. The tracking algorism determines the current position of the nanoparticle

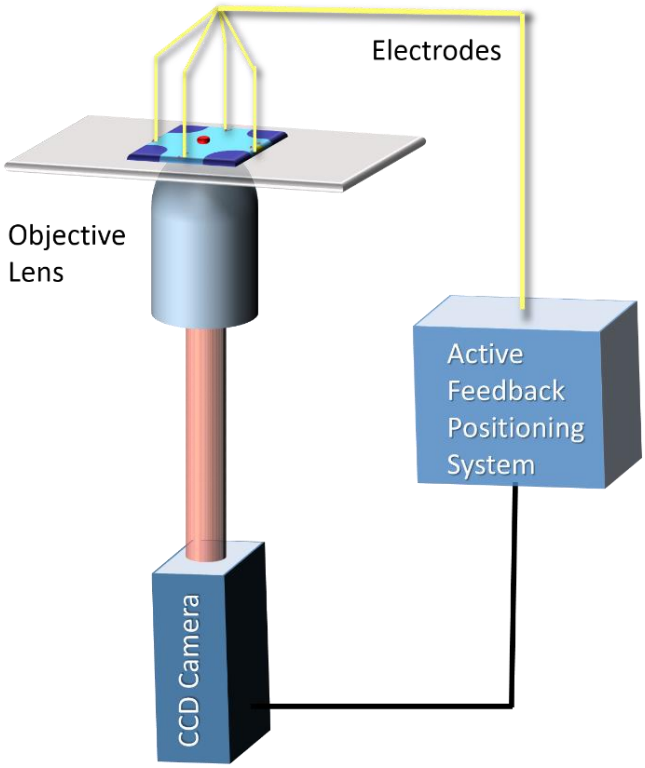

Figure 3: Illustration of active feedback positioning system. The control algorithm analyzes the image of the nanoparticle and control the nanoparticle by applying voltages to the electrodes.

in real time by fitting the CCD image to a point-spread function [21]. The control algorism, then compares the current position of the nanoparticle to the desired location and calculates a combination of four voltages required to actuate the nanoparticle. By applying appropriate voltage to each electrode, the positioning technique is enable to move the selected nanoparticle to the desired location [57]. This process can go into a continuous loop and repeatedly control the nanoparticle to trace a predefined path or to hold at a place with nanometric precision [54].

1.4 Nitrogen-vacancy color center

1.4.1 Overview

Diamond is the hardest material due to the tetrahedral structure of carbon atoms. There is a wide variety of atomic defects in diamond crystals with unique properties. The nitrogen-vacancy (NV) color center is one of atomic defects in diamond crystal structure. Two adjacent carbon atoms are removed from the diamond lattice and a nitrogen atom occupies one site while the other site is vacant (Figure 4). Involving an additional electron in the vacancy site, the six electrons associated make the NV center as a spin $S = 1$ system. The negatively charged NV center is notably studied throughout this thesis and NV center will refer to the negatively charged state.

The NV center can occur naturally or artificially in the diamond crystals. Since nitrogen is the most abundant element, nitrogen is also the most common impurity in natural diamonds. To engineer concentration of NV centers in diamond, nitrogen impurities are introduced to the diamond crystals by doping the CVD grown diamonds [58-60] or ion implantation [61-63]. However, a small fraction of nitrogen impurities creates a form of NV centers [64]. Annealing process enhances the probability of NV centers by diffusing vacancies to the nitrogen impurities [65, 66].

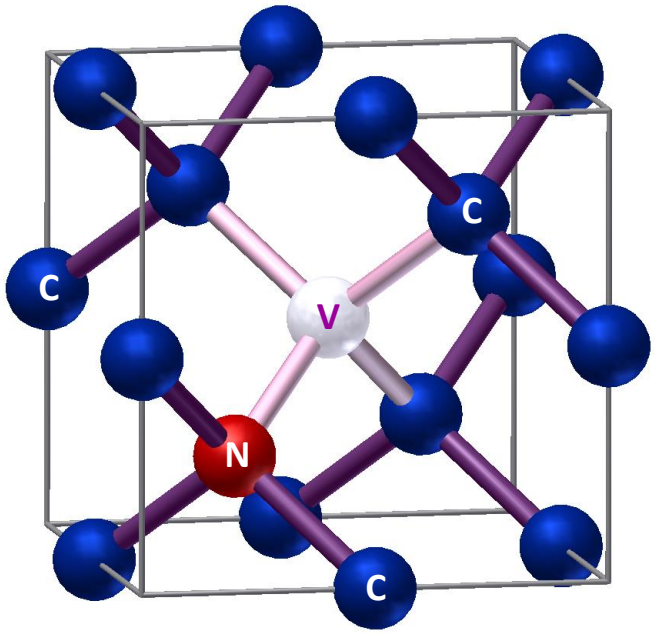

Figure 4: Atomic structure of the NV center in diamond lattice. The blue spheres with letter of “C” are carbon atoms. The red sphere with letter of “N” represents a nitrogen atom and the white sphere with letter of "V" indicates the vacancy site.

The NV center has been extensively investigated due to the remarkable properties. The NV center is a single photon emitter and shows reliable photo stability, unlike other fluorophores such as quantum dots and dyes [67, 68]. The NV center has a spin-triplet state with long spin coherence time, even at room temperature [69, 70]. The spin states are optically addressable [71, 72]. There are advantages inherited from diamond such as hardness and chemical and thermal stability, which make the NV center biocompatible [73]. The NV center can occur in any size and shape of diamond. These

advantages make the NV center as a promising platform for quantum information, biotechnology and quantum sensing.

1.4.2 Electron spin resonance

To understand electron spin properties of the NV center, this thesis discusses a simplified energy level structure of the NV center (Figure 5). The NV center works as three level system. The energy level structure of the NV center is consist of a spin triplet ground state, excited bright state and excited dark state. In the ground state,

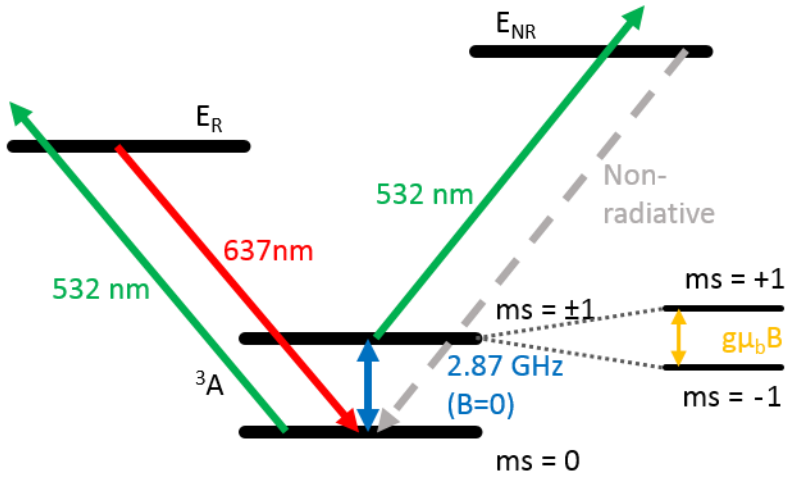

Figure 5: Simplified energy level structure of the NV center. The ground state is a spin-triple and shows a zero-field splitting of 2.87 GHz between the $m_s = 0$ and the $m_s = \pm 1$ states. The excited bright state is separated from the ground states by 637 nm. Zeeman effect splits $m_s = \pm 1$ states into two directly proportional to the external magnetic field B, where the $g = 2$, electron g-factor and μ_b is Bohr magneton.

there is a zero field splitting (D ≈ 2.87 GHz) between the $m_s = 0$ and the $m_s = \pm 1$ due to spin-spin interactions.

The NV center has a strong optical transition between the ground $m_s = 0$ state and the excited bright state with a zero phone line at 637 nm. However, there is a non-radiative transition associated with the excited dark state. Under optical excitation, electrons from the ground $m_s = \pm 1$ state decay non-radiatively toward the ground $m_s = 0$ state through the excited dark state. As a result, the ground spin state is polarized to the $m_s = 0$ state with the unpopulated $m_s = \pm 1$ state.

Microwave signal corresponding to the electron spin resonance (ESR) frequency pumps electrons from the $m_s = 0$ state to the $m_s = \pm 1$ state. This microwave transition causes an increase of non-radiative decay through the excited dark state. Under constant power excitation laser, applying microwave signal results in reduction of photoluminescence intensity of the NV center due to the non-radiative decay path. Therefore, scanning microwave frequency enables to optical detection of the spin states. Figure 6 shows measured fluorescence intensity of the NV center as a function of the microwave frequency. When the microwave signal is on resonance with the NV center, the fluorescence intensity is reduced.

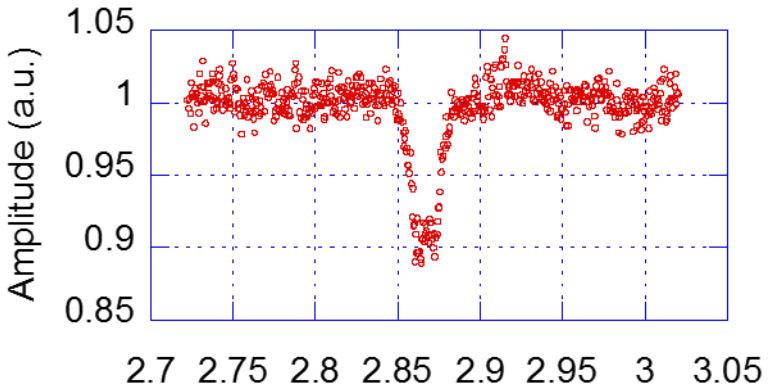

Figure 6: ESR spectrum of a single NV center without external magnetic fields. PL intensity of the NV center is reduced at electron spin resonance frequency of 2.87 GHz. The negative peak is separated due to the strain in diamond nanocrystal.

1.4.3 Optical magnetometry

The two ground $m_s = \pm 1$ states are indistinguishable and degenerate in energy at zero magnetic field. When external magnetic fields are applied to the NV center along the direction of the nitrogen to the vacancy, the degeneracy of two spin states is lifted. The Zeeman effects separate the ground $m_s = \pm 1$ state into two directly proportional to the magnetic field intensity. There are two electron spin resonance frequencies corresponding to the two spin states distinguishable in energy. Figure 7 shows optically detected electron spin resonance with a constant external magnetic field. The two microwave frequencies at the minimum fluorescence intensity indicate the two ground

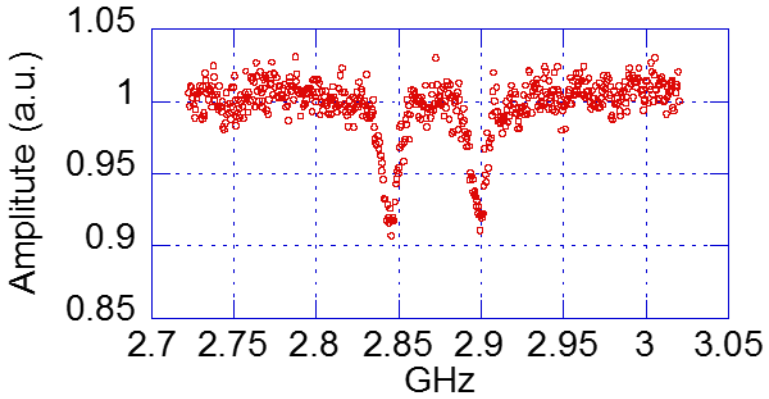

Figure 7: ESR spectrum of a single NV center with static external magnetic field. PL intensity of the NV center is reduced at two different spin resonance frequencies. The frequency separation between the two negative peaks is proportional to the applied magnetic field.

spin states split by Zeeman effects. We can detect the applied magnetic field to the NV center by measuring the frequency separation of the two spin states.

These properties enable highly sensitive NV-based magnetic field sensors with nanoscale spatial resolution [74-78], in contrast to other types of magnetic field sensors that achieve excellent field sensitivity but whose size is typically on the order of tens of microns or larger [79-81]. NV magnetometry has been deployed in a variety of applications such as detection of nanomechanical oscillations [82], readout of magnetic data [83, 84], monitoring ion concentrations [85-87], and magnetic imaging [88, 89]. NV centers in diamond are also bio-compatible [90-92] and can thus serve as biological sensors [93-95]. This capability has motivated recent efforts to manipulate and control a diamond nanocrystal hosting an ensemble of NV centers [96] and a single NV center [38] in a liquid environment using optical trapping techniques.

1.5 Outline of the Thesis

In this thesis, I present mainly two different applications using quantum probes combined with fluid flow nanoparticle positioning technique. Chapter 2 describes super-resolution imaging of a gold nanosphere using distortion information of far-field diffraction spot of a single quantum dot. Chapter 3 introduces a polarization dependent tracking technique for super-resolution microscopy of gold nanorods. Chapter 4 demonstrates a microfluidic device which is able to map the magnetic field profile of a magnetic nanoparticle using a single NV center. Chapter 5 presents a nanoscale magnetic sensing technique using ensemble of NV centers with CCD camera images. Chapter 6 concludes by discussing future applications of nanoscale sensing and imaging applications in a microfluidic device.

Chapter 2: Super-resolution imaging of gold nanosphere

2.1 Introduction

Super-resolution imaging of nanostructures often relies on the ability to track an emitter near a metallic or high dielectric surface. Such surfaces can significantly complicate the ability to precisely track a particle [97, 98]. Recent work demonstrated that near the surface of a silver nanowire, an emitter induces an image dipole that significantly distort the tracking accuracy [99]. Nanoparticles can distort the diffraction spots in even more ways, because they can efficiently scatter light that is hard to distinguish from the emitter itself. The effect of the nanoparticle on the tracking accuracy is difficult to study, however, because the actual position of the emitter is usually not known. For this reason it has been extremely difficult to ascertain the magnitude of these distortions.

In this chapter, we demonstrate that nanoparticles can significantly distort the tracking accuracy of a single emitter when performing super-resolution imaging. We develop a method that can systematically probe the distortion of an emitter's diffraction spot near a nanoparticle. This method allows us to quantitatively examine the distances as well as the directions of displacements in the centroid positions. We show that a nanoparticle can displace the diffraction spot of the emitter by more than 35 nm, which is much greater than the expected accuracy of the emitter tracking algorithm [100]. Large position displacement occurs even at distance of up to 300 nm from the nanoparticle position. Somewhat surprisingly, the presence of the nanoparticle causes the position of the emitter to appear pushed away from the surface. This result is

contrary to conventional wisdom that the emitter is a strong scattered that will pull the emitter's diffraction spot closer to the surface [36, 101, 102]. We use full-wave finite-difference time-domain (FDTD) calculations to show that this is indeed the expected behavior at large distances from the nanoparticle, while at very small distances the diffraction spot is pulled in due to bright nanoparticle scattering. Finally, we demonstrate that by monitoring the distortion of the diffraction spot we can perform highly accurate imaging of the nanoparticle. Our results provide a better fundamental understanding of near-field coupling between emitters and nanostructures and offer a promising route towards highly accurate super-resolution imaging of nanostructures.

2.2 Description of imaging approach

Figure 8 illustrates our measurement approach. We immobilize a single emitter on the surface of a microfluidic channels. In this way, we can ensure the actual position of the emitter. We manipulate a metallic nanoparticle suspended in the microfluidic channels near the immobilized emitter. In order to position the nanoparticle, we use

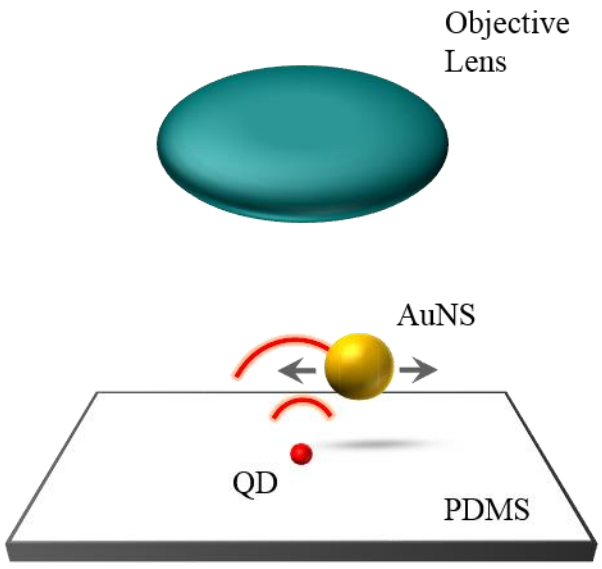

Figure 8: Schematic of experimental setup. A single quantum dot (QD) is immobilized on the PMDS surface of a microfluidic device. A gold nanosphere (AuNS) with diameter of 150 nm is controlled near the QD along the PDMS surface using fluid flow positioning technique. An objective lens is placed outside of the microfluidic device and collects the photoluminescence signals from both of the QD and the AuNS.

microfluidic flow control [57]. This technique enables us to position the nanoparticle with nanoscale accuracy by controlling the surrounding fluid. We then track the position of the emitter as a function of the position of the nanoparticle. This measurement approach enables us to observe any distortion to the centroid position induced by the presence of the nanoparticle.

2.3 Experimental procedure

In our experiments, we define microfluidic channels with a molded block of polydimethylsiloxane (PDMS) attached on a glass cover slip. We deposit a dilute concentration of quantum dots (CdSe/ZnS) on the PDMS surface by a spin-coating method. We then fill the microfluidic channel with the viscous fluid containing suspended gold nanospheres with average diameter of 150 nm. Our engineered fluid pushes the suspended gold nanospheres to the PDMS surface where the quantum dots are located. We employ a vision-based feedback control system to deterministically position the gold nanosphere at various locations close to the quantum dot along the PDMS surface. We have described the full details of the microfluidic device and the fluid flow control approach in previous works [54, 55, 103].

In order to track the position of the quantum dot and gold nanosphere, we use a home-built inverted wide field microscope. We illuminate the sample and collect emission with a 100x oil-immersion objective with a numerical aperture of 1.45. We excite the quantum dot with a 532 nm laser and collect the fluorescence emission at around 620 nm. We image the nanosphere using a halogen white-light source. We focus both the laser beam and the white light to illuminate a 20 μm diameter spot. We collect the resulting fluorescence with the same objective and project images of the two objects onto an electron multiplying charge coupled device (EMCCD) camera.

In order to monitor the distortion of the diffraction spot of the quantum dot induced by the gold nanosphere, we must accurately track both objects even when they are sufficiently close so that their diffraction spots overlap. To achieve this crucial requirement, we apply a stroboscopic imaging method. We interleave the white light and excitation laser, synchronized with the camera frame rate of 10 Hz, as depicted in Figure 9. When the white light is on and the excitation laser is off, we measure the position of the gold nanosphere. We subsequently turn off the white light and turn on the excitation laser to image the diffraction spot of the quantum dot. Both the excitation laser and white light illuminate the sample for a 50 ms duration. The two continuous images taken under different illuminations contribute a single measurement data point. By repeating this procedure, we can track the quantum dot and the gold nanosphere in

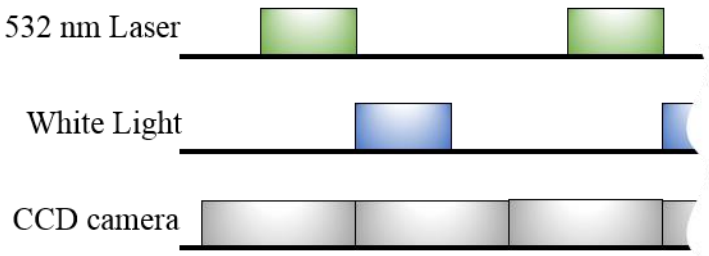

Figure 9: Measurement sequence of experiment. CCD camera is synchronized with 532 nm laser and white light. CCD camera exposes for 100 ms each frame and 532 nm laser and white light are opened for 50 ms.

the alternative camera frames and correlate the diffraction patterns of the quantum dot with the positions of the gold nanosphere.

Figure 10a,b are two consecutive camera images of an immobilized quantum dot and a nearby gold nanosphere (separated by 335 nm) taken under the excitation laser and the white light respectively. We focus on a 21 x 21 pixel area (~2.7 x 2.7 μm^2) around the collected emission or scatter signal and then fit each diffraction spot to a two dimensional Gaussian point-spread function to determine the centroid position. We indicate the centroid positions of the quantum dot (gold nanosphere) using a cross marker in green (blue). We do not observe any measureable signal from the nanosphere

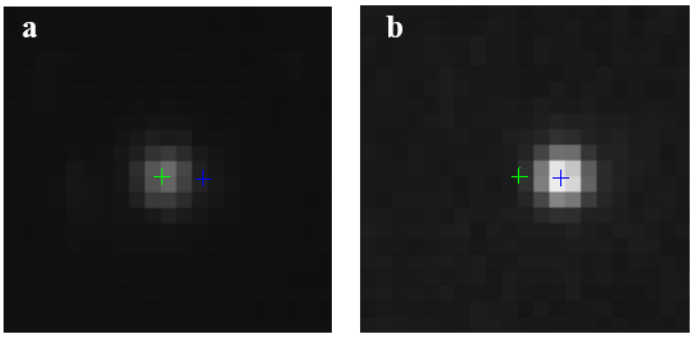

Figure 10: CCD camera images of QD and AuNS with excitation laser (a) and white light (b), respectively. Green cross marker represents the centroid position of QD and blue cross marker represents the position of AuNS. Distance between the QD and the AuNS is 335 nm.

when we image the quantum dot, nor do we observe any emission from the dot when imaging the nanosphere. We can therefore track both particles independently.

We determine the accuracy of the tracking algorithm by tracking positions of the immobilized quantum dot in the absence of gold nanospheres continuously for 4 minutes. Figure 11a is a scatter plot showing the accumulated centroid positions of the quantum dot in blue. Figure 11b,c plot a histogram of the measured quantum dot positions along the *x* and *y* coordinates respectively. By calculating the standard deviation of the histogram distribution, we determine the spatial precision of our tracking algorithm to be 8 (9) nm along the *x* (*y*) directions. This spatial precision is

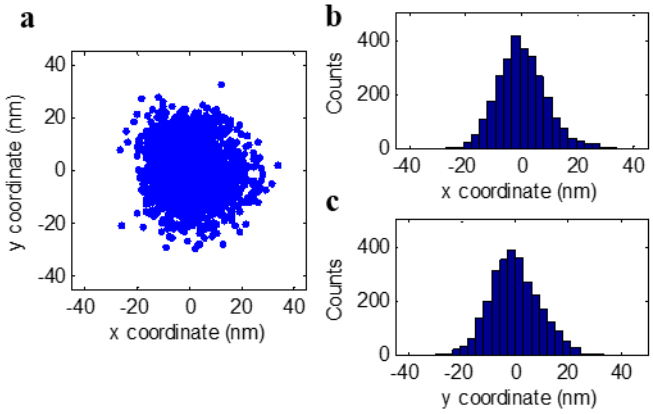

Figure 11: (a) Scatter plot of tracked positions of immobilized QD without AuNS nearby. Red circle represents actual position of QD. (b,c) Histogram of (a) along x (y) coordinates. Standard deviation is 8 (9) nm in x (y) axis.

limited by system vision noise, which includes a combination of camera read noise and multiplication noise, as well as shot noise of the emitter [33].

In order to probe the diffraction spot distortion induced by a gold nanosphere, we raster the position of the gold nanosphere over an area comprising a circle with a radius of 500 nm centered on the immobilized quantum dot. A set of scanning takes typically several tens of minutes. During this raster scanning, the mechanical vibration and the sample stage instability can cause slow drift of the microfluidic device resulting in inaccurate tracking of the emitter and the nanoparticle. To correct the sample drift, we use an immobilized gold nanoparticle as a position marker which is deposited on the PDMS surface prior the filling the microfluidic channels. We compensate the lateral position drift by tracking the position marker along with the quantum dot and the gold nanosphere simultaneously. We eliminate the effect of the vertical drift by filtering out the probing data when the position maker is out of focus. This three dimensional drift correction enables us to accurately probe the distortion of the diffraction spot. We apply the correction method throughout the experiment including the data shown in Figure 11.

In the tracking, we monitor the quantum dot and the gold nanosphere in alternative camera frames. Therefore, probing accuracy of our approach is highly related to how slowly move the gold nanosphere from one location to next location. We measure the positioning speed of the gold nanosphere in our probing measurements. We note that the positioning is performed uniformly over the probing area. The dominant

positioning speed is 7 nm/frame which is finer than the spatial imaging accuracy of 8 nm. 87 % of overall probing data is taken at the positioning speed slower than 14 nm/frame. The results ensure that we can track the quantum dot and the gold nanosphere simultaneously with spatial resolution well below the diffraction limit.

2.4 Displacement in centroid positions of emitter

We monitor the position of the quantum dot and the gold nanosphere to measure the diffraction spot displacement caused by the nanosphere. We define the displacement of the centroid position along the x and y axes as $\Delta x = \tilde{x} - x_0$ and $\Delta y = \tilde{y} - y_0$ respectively, where x_0 and y_0 are the x and y coordinates of the measured quantum dot position when the gold nanosphere is far away, and $\tilde{x}$ and $\tilde{y}$ are the x and y coordinates of the centroid position of the quantum dot. Figure 12a,b show the measured Δx and Δy as a function of the quantum dot position relative to the gold nanosphere is at the center. We also define the displacement distance as $\Delta r = \sqrt{\Delta x^2 + \Delta y^2}$.

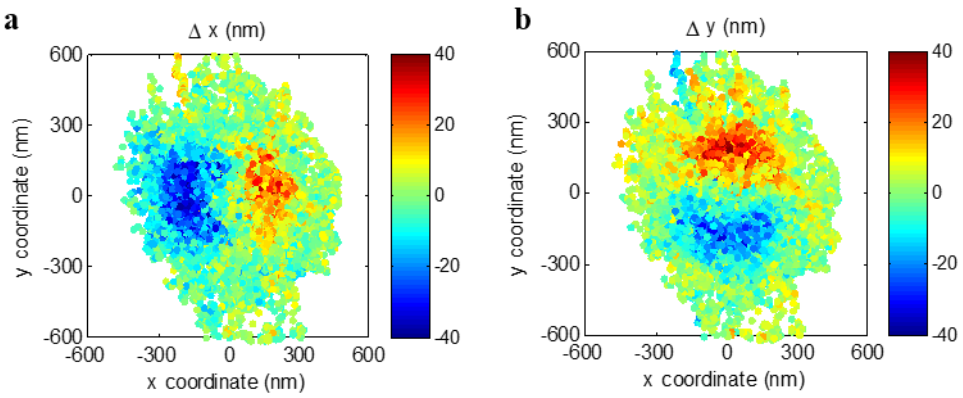

Figure 12: Scatter plot of measured Δx (a) and Δy (b) as a function of QD position relative to AuNS position respectively.

We generate reconstructed images by taking a Gaussian-weighted spatial average of the raw data shown in Figure 12. The Gaussian function is centered at the location of the pixel and the standard deviation is set to 8 nm, which is corresponding to the spatial precision of our tracking algorithm. Figure 13a-c are the reconstructed images of Δx, Δy and Δr as a function of the quantum dot position relative to the gold nanosphere at the center. The black lines indicate the surface of the gold nanosphere which corresponds to the typical diameter of 150 nm.

Figure 13a-b show that the quantum dot centroid can shift by more than 35 nm in the presence of the gold nanosphere. The centroid displacement occur even at distance of up to 300 nm from the gold nanoparticle position. The direction of the displacement is always away from the nanosphere, contrary to the apparent diffraction spot shifts towards the plasmonic structure which the emitter is coupled. Figure 13c plots Δr, which is symmetrical about the center position of the gold nanosphere, indicating that the diffraction spot always shifts away along the direction orthogonal to the surface of the gold nanosphere. This behavior is expected due to the rotational symmetry of the gold nanosphere geometry.

We compare our experimental results to numerical calculations based on finite-difference time-domain (FDTD) simulation. We simulate a gold nanosphere with 150 nm diameter and three dipole sources oriented orthogonal each other. The background index is set to 1.4 which corresponds to the refractive index of fluid and the PDMS. We monitor the radiation patterns of the dipoles by collecting the electric field within

in the collection angles of 1.45 numerical aperture. We repeat the FDTD simulation at various lateral distances between the dipole sources and the nanosphere, while keeping the vertical separation to 40 nm. Figure 13d-f plot the calculated results corresponding to the measurement data in Figure 13a-c. The numerical calculations show good agreement with the measured displacements profile at large distances from the gold nanosphere. The calculations show that at very close distances to the center of the gold nanosphere, the diffraction spot shifts towards the center of the gold nanosphere instead of being pushed away. We attribute this effect to large coupling strengths which induce bright nanoparticle scattering. Although we observe this displacement at very small distances (Figure 14), it is not noticeable in the color maps shown in Figure 13a-c due to the small contrast.

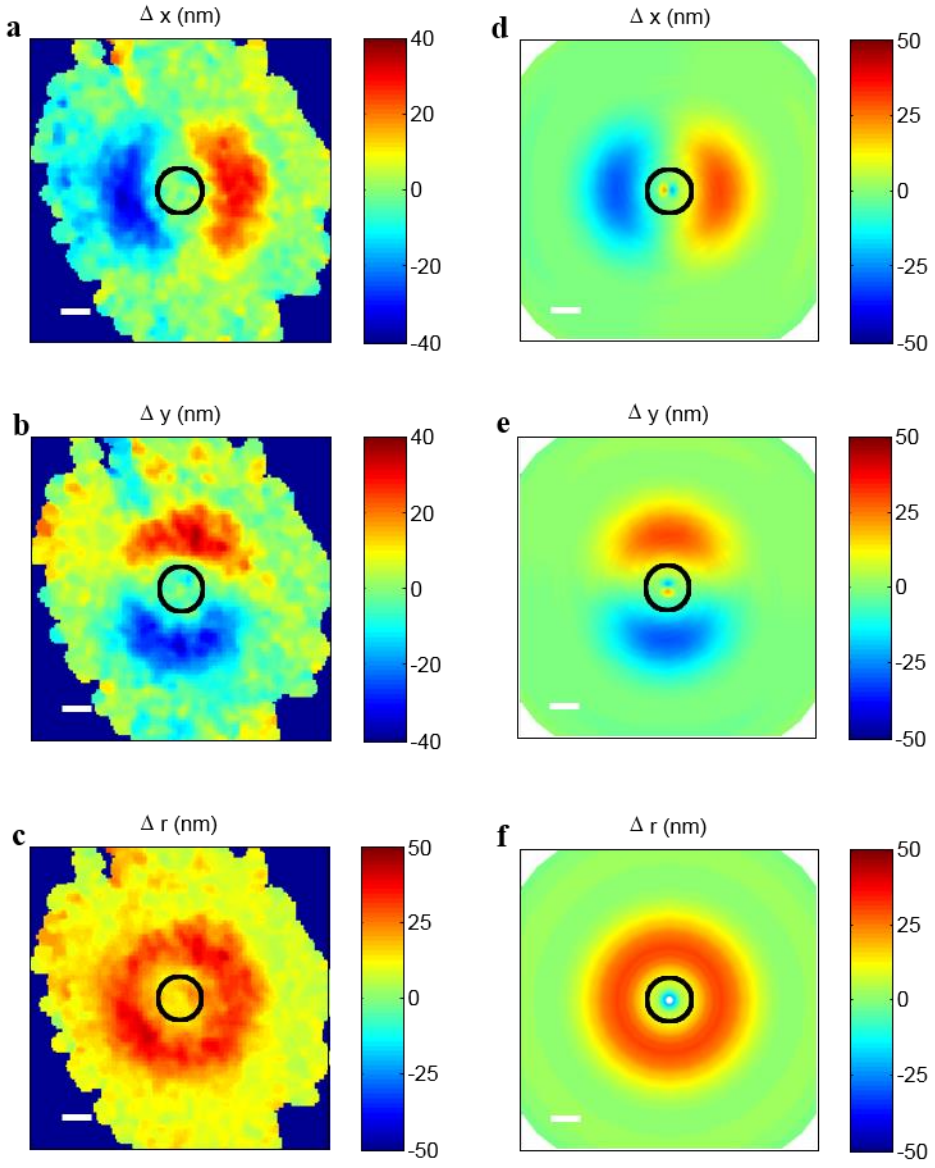

Figure 13: (a-c) Gaussian spatial averaged images of Δx (a), Δy (b) and Δr (c) as a function of QD position relative to AuNS position respectively. (d-f) FDTD simulation results corresponding to the (a-c) respectively. Scale bar is 100 nm. The black lines indicate the surface of the gold nanosphere with diameter of 150 nm.

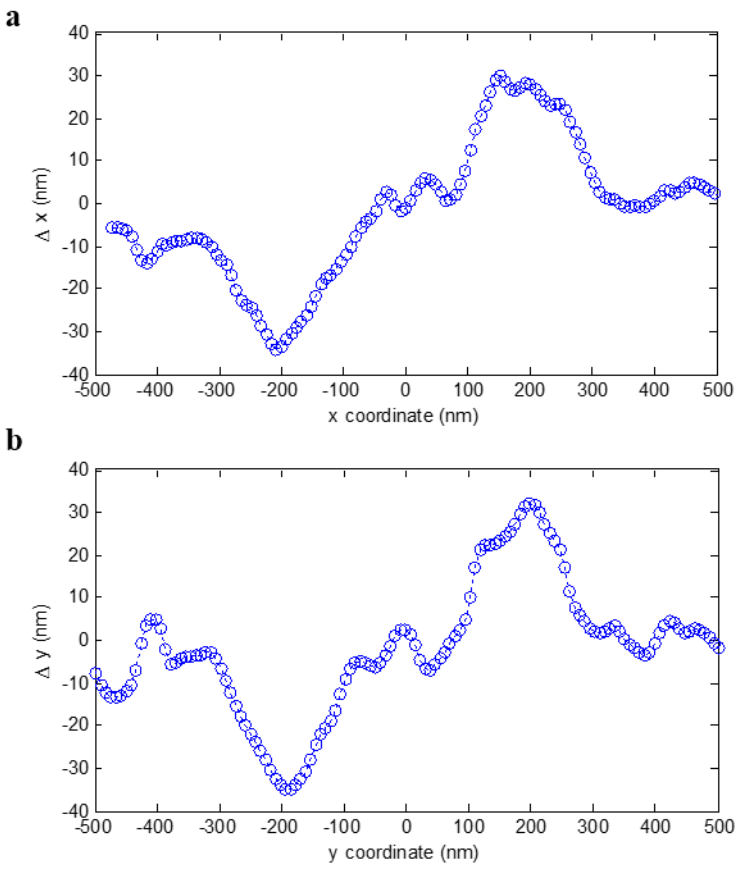

Figure 14: (a) Measured Δx along the x axis across the origin shown in Figure 13a. (b) Measured Δy along the y axis across the origin shown in Figure 13b.

2.5 Imaging of gold nanosphere with distortion of diffraction spot

Distortions to the diffraction spot can degrade the precision of super-resolution imaging techniques, but they may also contain useful information. In addition to the centroid positon displacement, tracking other aspects of the diffraction spot can be used to image the nanoparticle shape. We obtain the fluorescence intensity of the quantum dot by summing the CCD camera pixels within the tracking region shown in Figure 10a, while the full with half maximum (FWHM) of the diffraction spot is determined by the standard deviation of the Gaussian function which the diffraction spot is fitted. Figure 15a,b are the measured emission intensity of quantum dot and the FWHM of

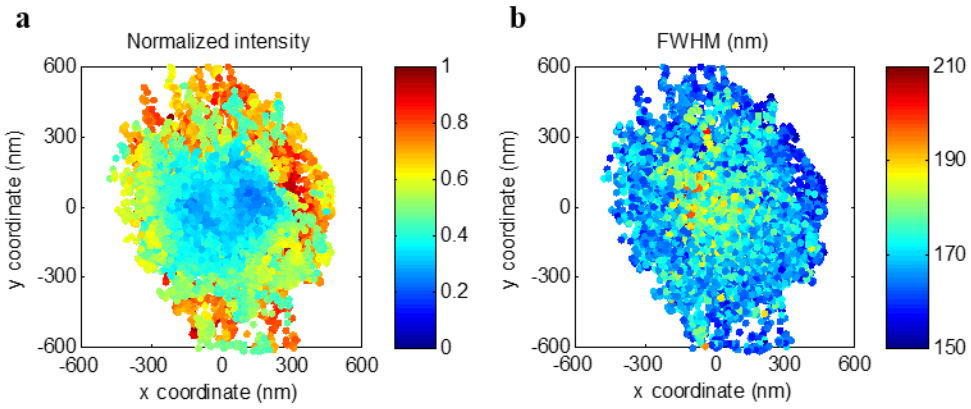

Figure 15: (a) Measured emission intensity and (b) FWHM of diffraction spot as a function of QD position relative to AuNS position respectively.

the diffraction spot as a function of the quantum dot position relative to the gold nanosphere at the center respectively.

We generate Gaussian-weighted spatially averaged images of measured emission intensity (Figure 16a) and diffraction spot size (Figure 16b) of the quantum dot respectively, using the raw data shown in Figure 15 in the same manner of Figure 13a-c. As the quantum dot goes behind of the gold nanosphere, the particle may shadow the quantum dot emission. Figure 16a,b show that the diffraction spot of the quantum dot appears dim and broaden when the quantum dot is cover with the nanosphere. This shadowing effect enable us to infer the shape and the size of the nanoparticle. Figure 16c,d plot the calculated FDTD results corresponding to the measurement data in Figure 16a,b respectively. The numerical calculations show good agreement with the measured shadowing effect from the gold nanosphere. We observe large fluctuations in both of the emission intensity and the diffraction spot size resulted from the quantum dot blinking [104]. We expect to achieve extremely fine images of the nanoparticle by using photo-stable emitters which can be predicted from the FDTD simulation results in Figure 16c,d.

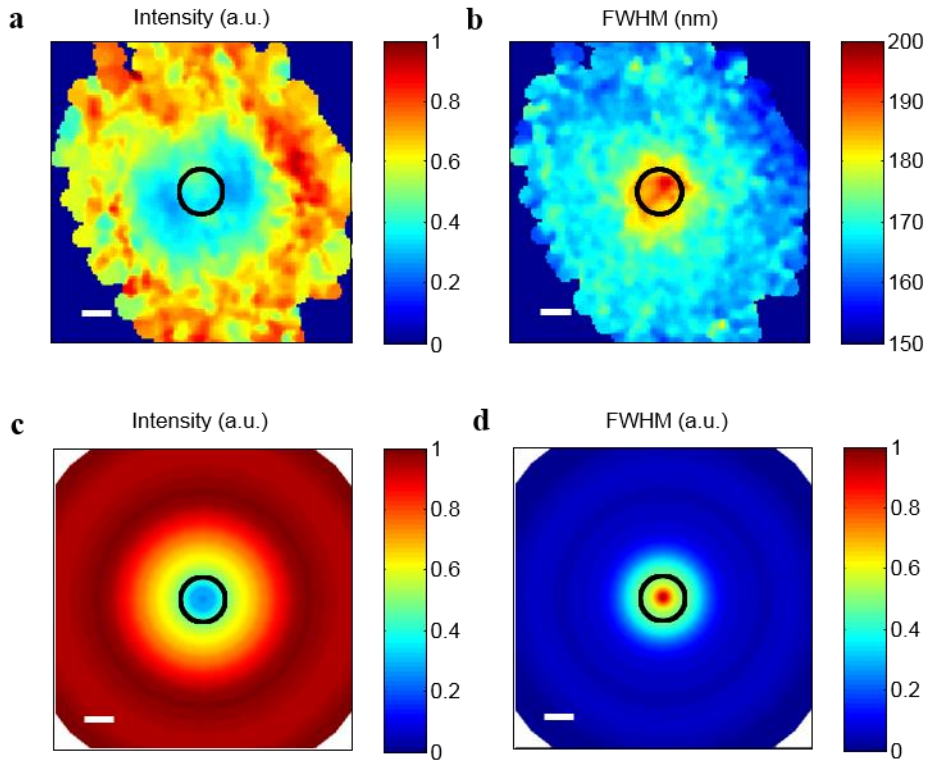

Figure 16: (a,b) Gaussian spatial averaged images of emission intensity (a) and FWHM of diffraction spot (b) as a function of QD position relative to AuNS position respectively. (c,d) FDTD simulation results corresponding to the (a,b) respectively. Scale bar is 100 nm. The black lines indicate the surface of the gold nanosphere with diameter of 150 nm.

2.6 Summery

In this chapter, we have demonstrated that the near-field coupling between an emitter and a nanoparticle can distort the far-field diffraction spot of the emitter. We manipulated a gold nanosphere near an immobilized quantum dot in a microfluidic device with nanoscale accuracy. By optically tracking the fluorescence images, we mapped out the distortion effect of the quantum dot by the gold nanosphere. We observed that the nanosphere shifts the centroid position of the quantum dot up to 35 nm, and the spatial displacements of the diffraction spot can occurs even at distance of up to 300 nm from the nanosphere position. Thus, our probing approach would enable to study the complex interaction between nanostructures and single emitters as well as optimize nanophotonic systems using single emitter tracking. Additionally, we have shown that the distortion of the diffraction spot is strongly position dependent. These results could open up new possibilities of nanoscale imaging applications using distortion information. This technique will provide an in situ super-resolution imaging of nanoparticles suspended in the fluid and a highly flexible imaging since it is free from special surface treatments. Although our results focused on the specific example of a gold nanosphere, this method can be applied to other shape of nanoparticle.

Chapter 3: Super-resolution imaging of gold nanorod

3.1 Introduction

We have demonstrated a new super-resolution imaging technique of single nanoparticle using distortion information of far-field diffraction spot of an immobilized single emitter in chapter 2. By positioning the nanoparticle near the emitter, this technique enables to study near-field interaction of light with nanostructures as well as image the nanoparticle with spatial resolution well below the diffraction limit. However, this technique is required to control a nanoparticle suspended in a microfluidic channel via fluid flow positioning. The suspended nanoparticle experiences diffusion motion in the fluid. The diffusion motion randomizes the orientation of the nanoparticles during the scanning and limits to apply this imaging technique to the non-spherical shape nanoparticles such as nanorods.

In this chapter, we develop a method of orientation tracking of single metal nanorods suspended in a microfluidic device. The nanorods exhibit a large plasmonic anisotropy in the longitudinal direction of the nanorods. By using polarization tracking, we precisely determine the orientation of the single gold nanorods. This optical orientation tracking method makes possible to apply the super-resolution distortion imaging technique discussed in chapter 2 to various anisotropic metal nanoparticles. Our finite-difference time-domain (FDTD) simulations show that the distortion of an emitter's diffraction spot near the surface of a gold nanorod could reveal structural information of the nanoparticle such as size and shape.

3.2 Plasmonic properties of gold nanorod

Metal nanoparticles exhibit surface plasmon resonance due to the electromagnetic fields localized near the surface of the particles [105, 106]. The shape of nanoparticles is one of the most important factors determining the surface plasmon modes of the nanoparticles. The metal nanorods show anisotropic plasmonic properties due to their elongated shape [36, 37, 107, 108]. In the optical excitation, conduction electrons oscillate along the long axis (longitudinal mode) and the short axis (transverse mode) of the nanorods [109]. The longitudinal modes exhibit resonance spectrum at a longer wavelenth than the transverse resonance mode [105, 106].

Figure 17 illustrates schematic of the excitation of longitudinal and transverse plasmonic modes, which correspond to the direction of L and W, respectively. Since the polarization of light strongly depends on the oscillation direction of excited electrons, the longitudinal mode is polarized along the long axis, while the polarization of transverse mode is parallel to the short axis of the nanorods [110]. By comparisons of polarizability of longitudinal and transverse modes, therefore, the optical detections provide the degree of alignment of the nanorods.

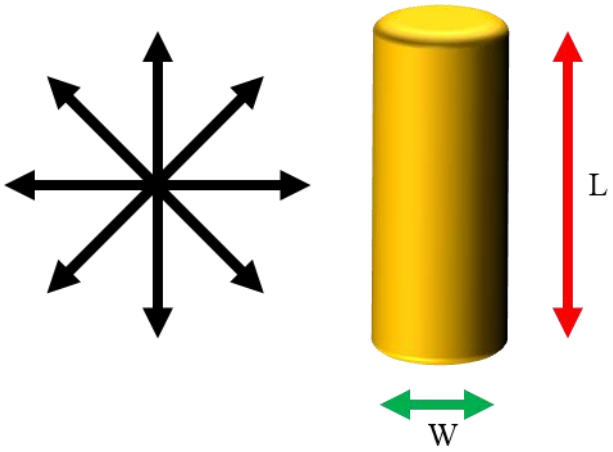

Figure 17: Illustrates of a gold nanorod and the excitation of longitudinal and transverse plasmonic modes, which correspond to the direction of L and W, respectively. Unpolarized excitation light is in black.

3.3 Polarization tracking of gold nanorod

In order to study the anisotropic surface plasmonic resonance effects of metal nanorods, we first examine a single gold nanorod deposited on a glass cover slip. We use gold nanorods with the average length and diameter of 180 nm and 45 nm, respectively. Due to the aspect ratio of 4.0, it has a longitudinal surface plasmon resonance at 800 nm and a transverse surface plasmon resonance at 527 nm. Since the transverse mode shows low intensity contrast and broad bandwidth, we focus on the longitudinal mode in the polarization measurements. We excite the longitudinal mode of the gold nanorod with an unpolarized light from a halogen lamp after pass through a band-pass filter with center wavelength of 800 nm and FWHM of 40 nm. An objective lens (100 ×, 1.45 NA) is employed to excite the gold nanorod and collect the strongly scattered light by the longitudinal plasmonic mode of the gold nanorod.

We use a birefringent calcite prism to separate the scattered light from a single gold nanorod into two orthogonal polarization directions and to get both polarization images simultaneously using a CCD camera. Figure 18 shows a CCD camera image containing two orthogonal polarizations of an isolated gold nanorod immobilized on a glass surface. We define $I_{\parallel}$ as a scattered polarization intensity parallel to the calcite prism orientation, whereas $I_{\perp}$ as a scattered polarization intensity perpendicular to the calcite prism orientation. We obtain the two orthogonal polarization intensities by summing the CCD camera pixels within independent two 21 x 21 pixel areas (~2.7 x 2.7 μm2) around the scatter signal shown in Figure 18.

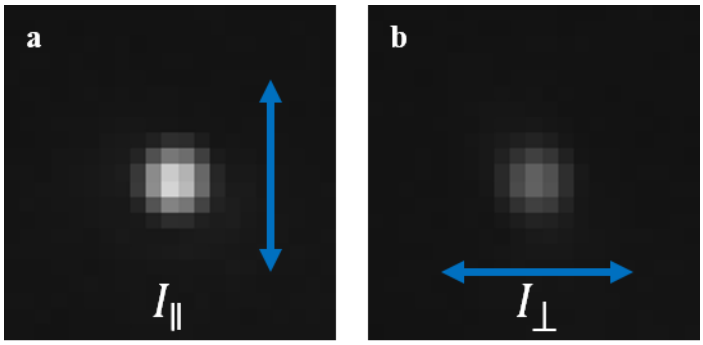

Figure 18: Polarization defendant CCD camera image of a gold nanorod. (a) Polarized parallel to the calcite prism orientation. (b) Polarized perpendicular to the calcite prism orientation. Blue arrow indicates the direction of polarization.

To quantify the polarizability of the scattered signal from a gold nanorod, we define the polarization anisotropy, $\mathrm{PA} = (I_{\parallel} - I_{\perp})/(I_{\parallel} + I_{\perp})$. The PA values can be between +1 and -1, depending on the calcite prism orientation relative to the direction of the nanorod. When the calcite prism orientation is aligned to the longitudinal (transverse) axis of the nanorod, it gives the maximum (minimum) PA value. Since we track two polarization intensities simultaneously, the polarization anisotropy is insensitive to the intensity fluctuations of the excitation light and the drift of the nanorods.

We analyze the emission properties of an immobilized gold nanorod by monitoring the polarization anisotropy when varying the angle of the calcite prism orientation.

Figure 19a is a polar plot of the polarization anisotropy PA as a function of the orientation angle of the calcite prism. It shows that the emission signal from gold nanorods is linearly polarized in the direction of the longitudinal axis. We calculate the orientation angle of the gold nanorod using the polarization anisotropy. Figure 19b a scatter plot of the polarization anisotropy PA versus the orientation angle of the calcite prism using the same date shown in Figure 19a. It shows that PA varies periodically. By fitting the data to a sinusoidal function, we determine the orientation angle of the gold nanorod as -31.5349˚ to the horizontal direction of the CCD camera with the 95% confidence of 0.0288˚. These results, therefore, show that we can determine the orientation angle of a gold nanorod with high precision.

We investigate rotational dynamics of the gold nanorods which is freely suspended in a fluid using the polarization anisotropy tracking technique. We fill a microfluidic channel with a DI water based solution containing gold nanorods. The detail of fluid solution is discussed in the chapter 1. We track a single gold nanorod while keeping the orientation of the calcite prism fixed throughout the measurements. Figure 20a shows a time trace of the polarization anisotropy for 100 sec. Our polarization anisotropy tracking technique enable to determine the orientation of the nanorod in real time.

Figure 20b shows normalized total intensity as a function of time by adding two orthogonally polarized intensities used in Figure 20a. The total intensity remains close to the maximum intensity most of the tracking times. It indicates that the orientation

of the gold nanorod is confined in the directions parallel to the PDMS surface of the microfluidic channel. As the angle between the orientation of gold nanorod and the PDMS surface increases, the excitation of the surface plasmon resonance mode would be significantly suppressed. We note that the confined 2D motion is attributed to the cetyl trimethylammonium bromide (CTAB) surfactant coated on the nanorods, which makes the nanorods positively charged [111].

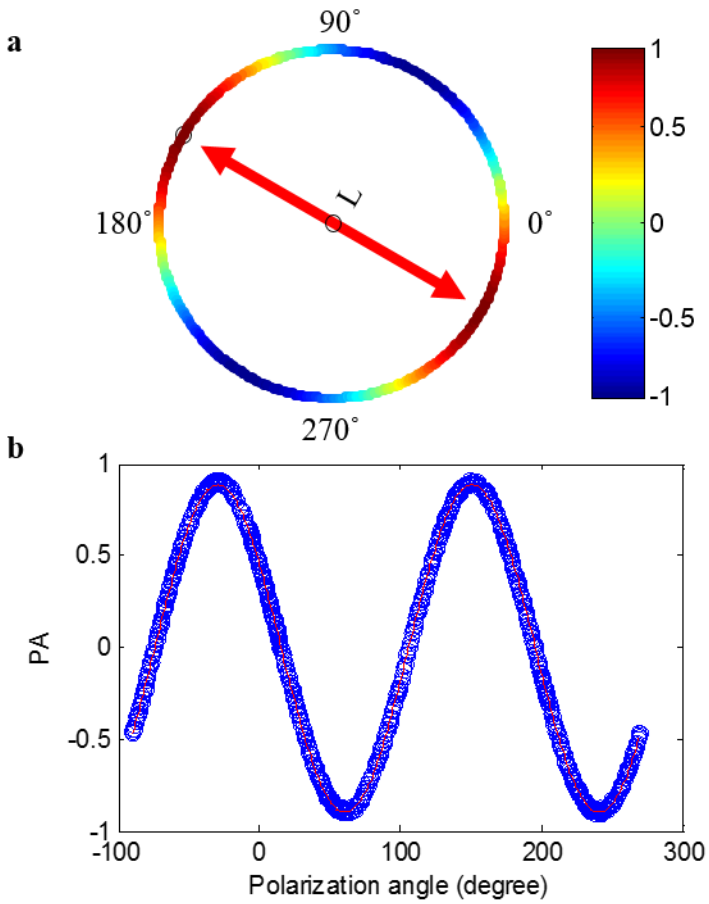

Figure 19: (a) Polar plot of the polarization anisotropy PA as a function of the orientation angle of the calcite prism. The red arrow represents the direction of the longitudinal axis of the gold nanorod. (b) The blue is measured polarization anisotropy PA as a function of the orientation angle of the calcite prism. The red curve is a fit to a sinusoidal function. The orientation angle of the gold nanorod is determined as -31.5349˚.

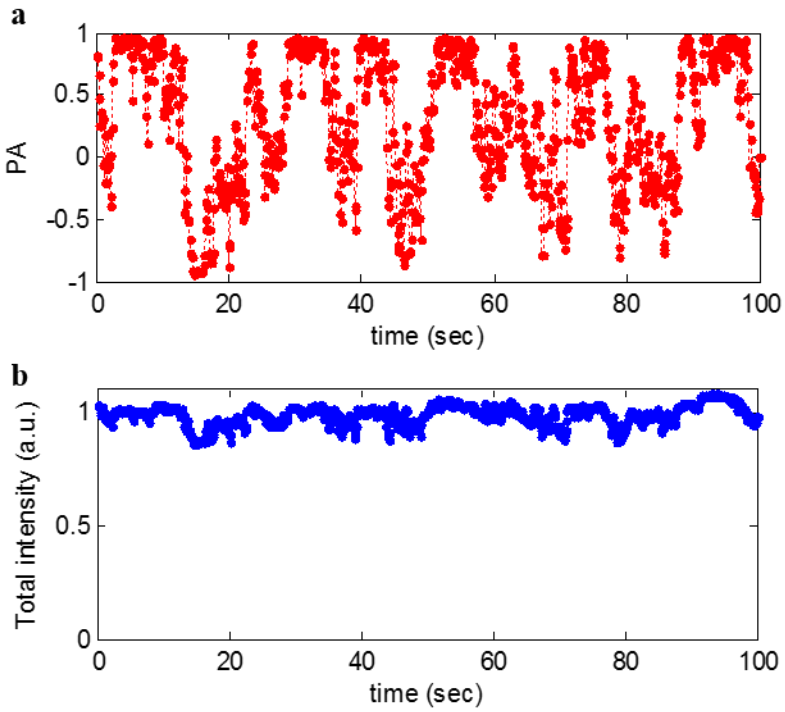

Figure 20: (a) polarization anisotropy PA of a gold nanorod suspended in the microfluidic channel as a function of time. (b) Total fluorescence intensity of the gold nanorod as a function of time. It is measured at the same time with the data shown in (a).

3.4 Imaging of gold nanorod with distortion of diffraction spot

Far-field diffraction spot of a nanoscale emitter in the proximity of a plasmonic nanoparticle can give us structural information such as shape and size of the nanoparticle. We use numerical finite-difference time-domain (FDTD) calculations to speculate the super-resolution imaging of a gold nanorod using diffraction spot distortion of a quantum dot. In the FDTD calculations, the gold nanorod (length of 200 nm, diameter of 50 nm) is surrounded by a background of 1.40 refractive index, which is close to the refractive index of the DI water based fluid and the PDMS microfluidic channel. We use a group of three dipole sources which is placed at same position and polarized orthogonally each other to simulate the quantum dot. We obtain diffraction patterns of the dipole sources using a far-field projection taking account of an objective lens of 1.45 Numerical Aperture. We repeat the FDTD simulations varying the position of the dipole sources with steps of 5 nm in XY plane, keeping the distance of 40 nm to the surface of the gold nanorod in the Z axis.

We extract the fluorescence intensity, the angle and the FWHM of the calculated diffraction patterns by fitting them to a two-dimensional Gaussian function. Figure 21a is a mapping of the fluorescence intensity on the positions of the dipole sources relative to the gold nanorod. When the dipole sources place behind the nanorod, the fluorescence intensity significantly decreases due to the shadow effect. The shape of emitter's diffraction spot is very sensitive to the near-field coupling to the nanostructure and can be used to reconstruct images of the structure. Figure 21b shows the angle and

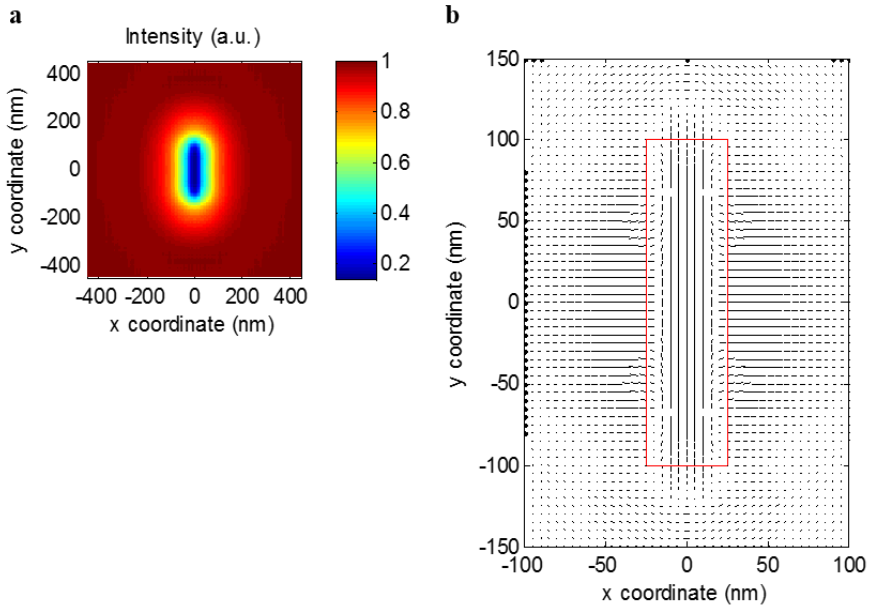

Figure 21: (a) polarization anisotropy PA of a gold nanorod suspended in the microfluidic channel as a function of time. (b) Total fluorescence intensity of the gold nanorod as a function of time. It is measured at the same time with the data shown in (a).

the FWHM of the diffraction patterns with vectors at the dipole positions. The direction and the length of vectors represent the angle and the FWHM of diffraction spot, respectively. The shape of diffraction spot of the emitter looks stretched along the longitudinal axis of the nanorod when it is under the nanorod, while the diffraction spot gets elongated orthogonal to the surface of the nanorod when it moves away from the surface.

3.5 Summery

In this chapter, we have demonstrated an imaging technique to precisely track the orientation angle of a gold nanorod utilizing polarization anisotropy. Using this technique, we have tracked rotational dynamics of the gold nanorods that is freely suspended in a microfluidic channel. This result opens up the possibility of the super-resolution imaging of non-spherical nanoparticle using the technique discussed in the chapter 2. We have provided FDTD simulation results that the fluorescence intensity and the diffraction spot shape of a probing emitter can reveal the shape and size of the nanorod. The super-resolution microscopy technique based on diffraction spot distortion of emitters is an excellent nanoscale imaging tool which can be applied to wide verity of nanoparticles.

Chapter 4: Nanoscale magnetic field detection using single NV center

4.1 Introduction

The integration of NV magnetometry with microfluidic systems could open up new possibilities for real-time biological and chemical sensing. Microfluidics provides an ideal device platform for sorting and manipulating samples using magnetic, optical, mechanical, or electrical methods [112, 113]. An important recent example is the work of Steinert et al. [114] that demonstrated a spin relaxometry technique based on an array of NV centers in a microfluidic device. This technique measured the concentration of a large ensemble of freely diffusing magnetic ions and molecules. However, the microfluidic device in that work was only used to prepare appropriate ion concentrations.

In addition to preparing fluid concentrations, microfluidics can also isolate and manipulate individual objects. For example, a variety of control methods based on electrokinetic [115-117] and magnetic tweezers [118-120] can manipulate objects inside a microfluidic device with nanometer spatial precision [33, 54, 55]. Combining these highly precise particle manipulation approaches with NV magnetometry opens up the possibility to map the magnetic field distributions of target objects with nanoscale accuracy, which is essential for a broad range of magnetic imaging applications [74, 75].

Here we demonstrate the ability to map the magnetic field of suspended objects in a microfluidic system with high nanometer spatial resolution and high sensitivity using

NV magnetometry. We manipulate a single magnetic particle in three dimensions using a combination of planar electroosmotic flow control and vertical magnetic actuation. A diamond nanocrystal containing a single NV color center acts as a localized magnetic field sensor for the manipulated magnetic particle. We measure the magnetic field generated by the magnetic particle via optically detected electron spin resonance (ESR) measurements, and map out its field distribution with nanoscale accuracy. In contrast to other scanning magnetometry methods based on AFM [76, 83], which require a complex experimental setup and are challenging to perform in liquids, our approach uses only simple optical microscopy and is naturally integrated into a microfluidic device. Our results thus open up the possibility for highly sensitive mapping of local magnetic field distributions in a fluid environment.

4.2 NV magnetometry microfluidic device

Figure 22 illustrates the microfluidic system we have developed to manipulate magnetic particles and perform localized magnetometry. The device is composed of two microfluidic channels formed between a glass cover slip (1 in x 1 in wide, 150 μm thick) and a molded block of polydimethylsiloxane (PDMS). The microfluidic channels are filled with a viscous fluid that contains target magnetic particles in a liquid suspension. In addition to increasing the fluid viscosity, the fluid also serves to push the magnetic particles to the surfaces of the device [33, 55]. We find that the magnetic particles are preferably confined at the top PDMS surface of the microfluidic channels.

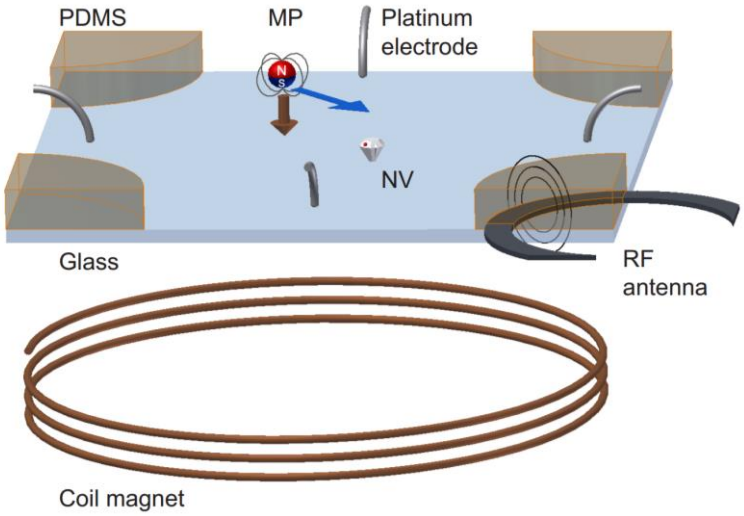

Figure 22: Schematic of microfluidic device used to implement NV magnetometry. The magnetic particle is labeled by "MP".

The intersection between the two channels forms the control chamber where we manipulate particles and map their magnetic field distribution.

We manipulate particles in the plane of the microfluidic device by applying voltages at the four ends of the microfluidic channels and using feedback control [33, 54, 55]. The voltages induce electroosmotic flow that moves the suspended magnetic particle towards desired directions by viscous drag. To achieve vertical manipulation, we use magnetic actuation. We place a coil magnet under the microfluidic device that applies a magnetic field in the vertical direction. The magnetic field provides a downward force on the magnetic particle, and also orients its dipole moment along the vertical direction.

In order to perform local magnetometry, we deposit a dilute concentration of diamond nanocrystals (mean size of 25 nm) on the glass surface of the microfluidic device using a spin coating method. These diamond nanocrystals serve as local magnetic field sensors. We lithographically pattern a microwave antenna (500 nm Au, 10 nm Ti) on the glass cover slip surface in order to drives the spin transition of the NV center to perform optically detected ESR measurements [74]. Figure 23a shows an optical image of the microfluidic device with the integrated microwave antenna. We align the microfluidic channel such that the microwave antenna is as close as possible to the control chamber without directly penetrating into it. A tunable microwave signal generator (ROHDE&SCHWARZ SMC100A) drives the antenna over a spectral range that spans the entire ESR resonance of the NV center (centered at 2.863 GHZ).

We mount the microfluidic device on an inverted confocal microscope system that excites and collects emission from a NV center and images a manipulated magnetic particle through the bottom glass cover slip using a 1.45 numerical aperture oil immersion objective. A piezo stage attached to the microscope enables precise translation of the microfluidic device in three dimensions. We excite the NV center using a 532 nm continuous wave laser and use a half-waveplate to rotate the polarization to achieve maximum fluorescence intensity. In addition to the excitation laser, we use a white light source to image the magnetic particle. The excitation laser beam is tightly focused onto the NV center while the white light beam is widely focused to a 20 μm diameter.

A beamsplitter sends 25% of the collected light to an EM-CCD camera (Hamamatsu C9100-13) to track the magnetic particle using a 10 Hz camera frame rate. Figure 23b shows an EM-CCD camera image of a single diamond nanocrystal and a nearby magnetic particle in the control chamber of the microfluidic device. For all experiments reported in this chapter the magnetic particles are spherical maghemite magnetic beads with a radius of 500 nm (Chemicell, Germany). The green and red boxes highlight the diamond nanocrystal and the magnetic particle respectively. We select a diamond nanocrystal located close to the patterned microwave antenna in order to minimize the microwave power required to excite ESR transitions.

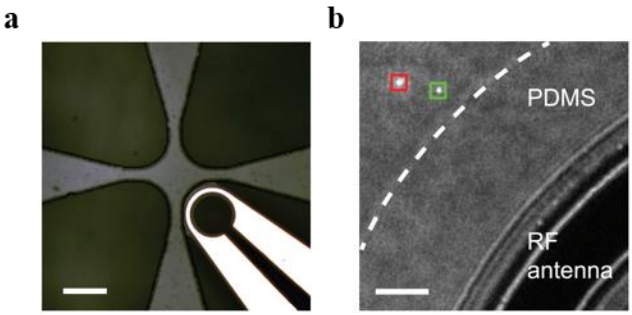

Figure 23: (a) Optical image of the control chamber of the microfluidic device along with integrated microwave antenna. Scale bar is 100 μm. (b) EM-CCD image of an immobilized NV center (green) and a suspended magnetic particle (red) inside the microfluidic control chamber. The white dashed line represents the boundary between the fluid and the PDMS sidewall of the channel. Scale bar is 5 μm.

The remaining 75% of the collected light is spatially filtered by a pinhole aperture and spectrally filtered using a 600-750 nm bandpass filter. This combination of spatial and spectral filtering isolates the emission from the NV center and rejects the background signal from the scattered white light with a high extinction ratio. The filtered NV emission is directed to an avalanche photodiode (PerkinElmer SPCM-AQR) to perform optically detected ESR measurements. The signal can also be directed to a Habury-Brown Twiss (HBT) intensity interferometer composed of a 50/50 beam-splitter and two avalanche photodiodes, to perform second order correlation measurements. A time interval analyzer (PicoQuant PicoHarp 300) performs time-

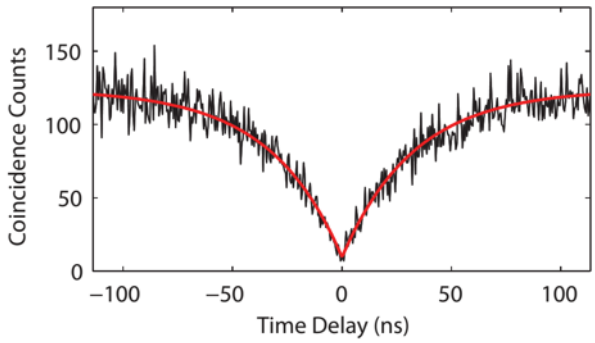

Figure 24: Second order correlation measurement of a single NV center in a diamond nanocrystal.

resolved coincidence detection using the outputs of the two photon counters. Figure 24 shows an autocorrelation measurement taken from the diamond nanocrystal that exhibits clear anti-bunching, indicating that it contains only a single NV defect.

4.3 3D magnetic nanoparticle positioning

We first investigate the ability to manipulate a magnetic particle within the microfluidic control chamber. Figure 25(a-c) shows a sequence of camera images of a single magnetic particle that we manipulate on the PDMS surface to undergo a square spiral trajectory using feedback control. The panels show the position of the particle at three different times (150, 300, and 450 sec). The cyan and magenta boxes indicate the start and stop positions of the trajectory. The white line shows the past history of the measured positions of the controlled particle.

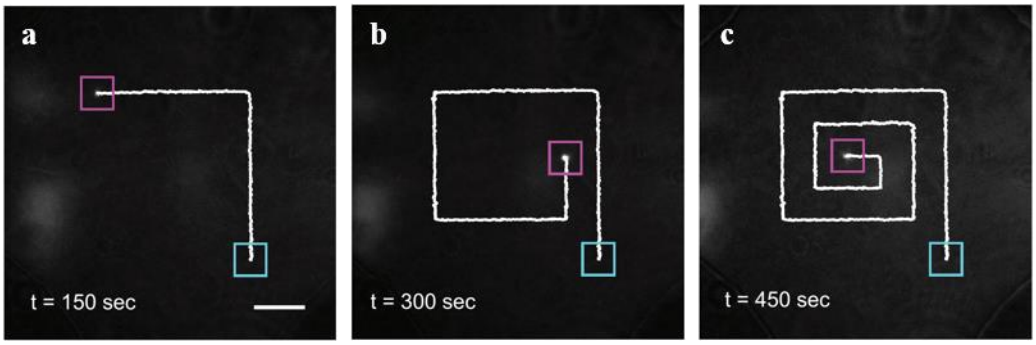

Figure 25: Camera images of a magnetic particle manipulated along a 2D square spiral trajectory. The cyan box indicates the start position of the selected magnetic particle, and the magenta boxes indicate the stop location of the particle at (a) 150 s, (b) 300 s, and (c) 450 s respectively. The white line shows the past history of the measured positions. Scale bar is 10 μm.

In order to determine the positioning accuracy we hold the particle at a desired location for 60 seconds and continuously monitor its position. Figure 26a shows a two-dimensional plot of the measured positions, and Figure 26b,c show position histograms along x and y direction respectively. We fit each histogram to a Gaussian (red solid line) and determine a standard deviation of 48 (47) nm along the x (y) directions respectively.

To achieve motion of the magnetic particle in the direction orthogonal to the surface, we apply a current to the coil magnet under the device. The generated magnetic field applies a force that pulls the magnetic particle away from the PDMS surface and towards the glass surface. Figure 27 plots the measured distance of the magnetic

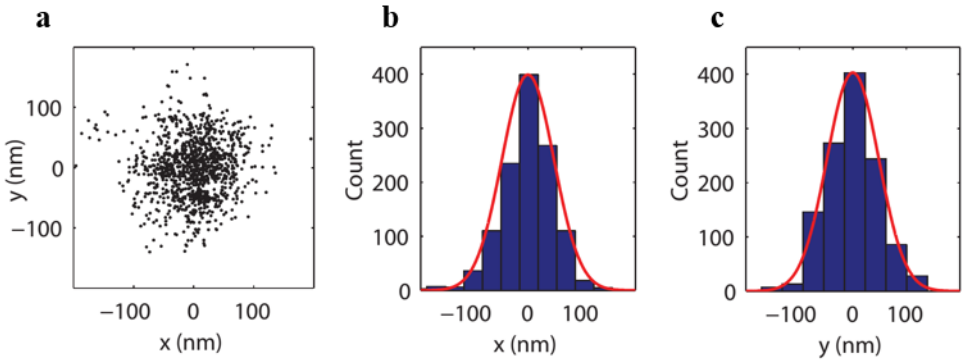

Figure 26: (a) Scatter plots of the measured positions of the magnetic particle held in place using flow control for 60 sec. (b,c) Position histograms along the x and y axes of panel a. The solid lines are Gaussian fits to the position histograms. The standard deviation is 48 (47) nm along the x (y) directions respectively.

particle to the bottom glass surface as a function of the current driving the coil magnetic. We measure this distance by sweeping the particle through the focus of the objective lens using the piezo stage that holds the microfluidic device. We determine the focused position from the minimum spot size and record the stage travel distance. We repeat the measurement five times for each value of the external current. The blue dots in Figure 27 show the values obtained for the five individual measurements, while the red line shows the average value of the data.

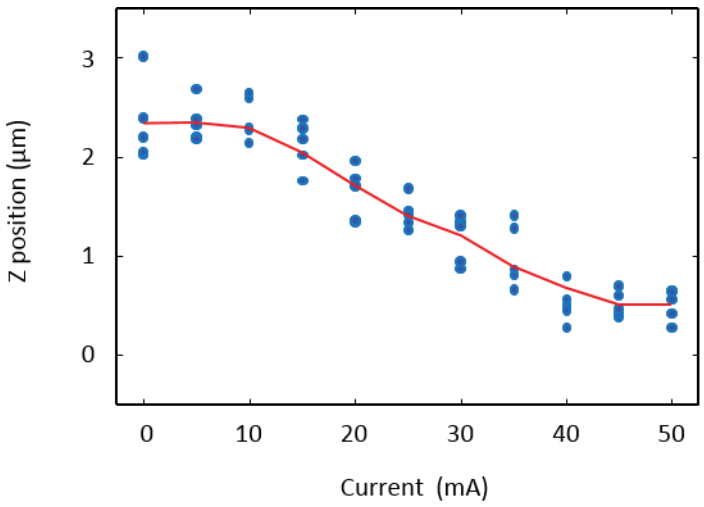

Figure 27: Vertical distance of the magnetic particle relative to the bottom glass surface as a function of the current driving the coil magnetic underneath the device. Blue dots show individually measured values while the red line shows the averaged values.

At each driving current, the magnetic particle stabilizes at a different distance relative to the bottom glass surface due to cancellation between fluid forces that push the particle upwards to the top PDMS surface, and magnetic gradient forces that pull it downwards towards the bottom glass surface. This interplay between chemical buoyancy versus magnetic downward force enables us to control the vertical position of the magnetic particle relative to the device surface. At 40 mA current, the particle is pulled almost all the way to the bottom glass surface. The applied magnetic field also serves to orient the dipole moment of the suspended magnetic particle along the direction of the applied field in the fluid, thereby eliminating the effect of tumbling of the particle that would otherwise randomize its orientation relative to the measurement direction of the NV center.

4.4 Mapping magnetic field profile of magnetic nanoparticle

In order to measure the magnetic field generated by the magnetic particle, we scan its position relative to the NV center and perform optically detected ESR measurements. We isolate a diamond nanocrystal that contains a single NV center on the glass surface in the control chamber. We apply a 50 mA current to the external coil magnet in order to pull the magnetic particle down to the glass surface where the NV center is located. Based on this current and the measurement results in Figure 27, we estimate the center of the magnetic particle to be located 0.7 μm above the glass surface. Under these conditions, we scan the magnetic particles position relative to the NV center and obtain an ESR spectrum at each position.

We perform the ESR measurements using a digital lock-in approach, as originally proposed by Horowitz *et al.* [96]. This technique eliminates photoluminescence intensity fluctuations that arise slow mechanical drift of the NV center relative to the tight Gaussian excitation laser, instability of the NV center emission caused by charge fluctuations on the surface [96, 121], and other slow intensity fluctuations induced by the microfluidic environment. We perform lock-in by modulating the microwave power supply on and off at a 1 KHz rate and measuring photoluminescence intensity synchronized with this modulation. We define the photoluminescence intensity contrast of the NV center as

$$C(f) = \frac{N_{on}(f) - N_{off}(f)}{N_{off}(f)}, \quad (2)$$

where N_{on} and N_{off} are the measured photon counts when the microwave is on and off respectively at each value of the microwave frequency.

Figure 28 shows the ESR spectrum of the NV center taken at three different positions of the magnetic particle. The left panels show the measured ESR spectrum, where blue dots represent measured data points and the red lines are Lorentzian fits to the measured data. The right panels show EM-CCD camera images that indicate the horizontal position of the magnetic particle (red box) and the NV center (green box).

Panel a shows the case where the magnetic particle is 7.25 μm away from the NV center so that its contribution to the total magnetic field is negligible. The two ESR peaks correspond to the Zeeman split spin ground states of the NV center which are separated by 42.3 MHz. This large splitting is due to the applied magnetic field from the external coil magnet. As we bring the magnetic particle to a distance of 3.62 μm (panel b), the Zeeman splitting reduces to 40.7 MHz because the field generated by the magnetic particle opposed the external field of the coil magnet. This change in Zeeman splitting provides a direct quantitative measure of the magnetic field given by the magnetic particle. At an even shorter distance of 1.50 μm (panel c), the Zeeman splitting is further reduced to 34.2 MHz.

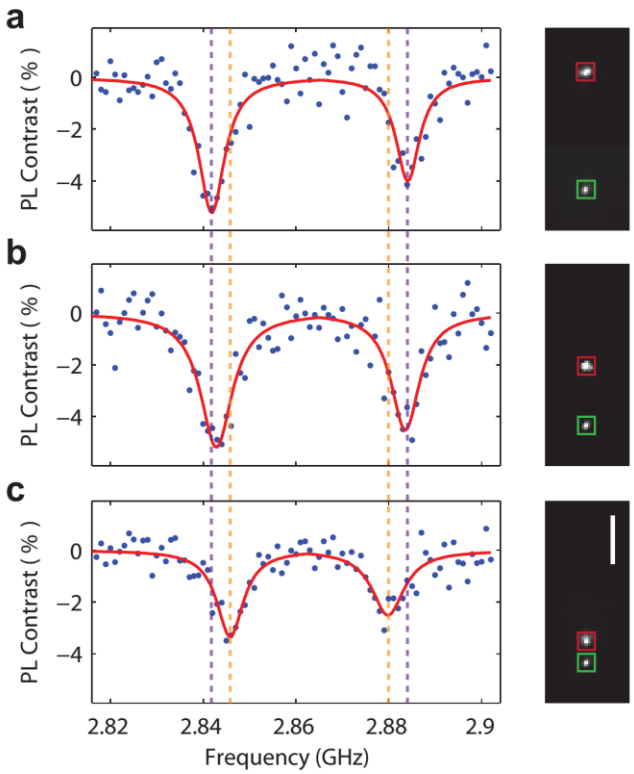

Figure 28: Optically detected ESR spectra (left) and camera images (right) of the magnetic particle (red square) and NV emission (green square) when the particle is at a distance of (a) 7.25 μm, (b) 3.62 μm, (c) and 1.50 μm from the NV center. Scale bar is 3 μm. The red lines in the spectra are Lorentzian fits to measurement data. Dashed lines in purple and orange are the center frequencies of the Lorentzian fits in (a) and (c).

Because our system operates close to the shot noise limit, we can estimate the magnetic field sensitivity of our magnetometry system using the shot-noise limited relation [74, 122]

$$\eta_B = 0.77 \frac{h}{g\mu_B} \frac{\Delta\nu}{C\sqrt{R}}, \quad (3)$$

where h is the Planck constant, $g = 2$ is the Lande g-factor for the NV center, and μ_B is the Bohr magneton. Using the data in Figure 28a, we calculate a maximum photoluminescence intensity contrast of $C = 0.053$, along with a hyperfine unresolved microwave ESR linewidth of $\Delta\nu = 7.2$ MHz. The fluorescence count rate is measured to be $R = 45$ kCts/s. Inserting these values into Equation 3 we attain an estimated magnetic field sensitivity of 17.5 μT $Hz^{-1/2}$. This result compares well with previously reported magnetic field sensitivities of NV magnetometry demonstrated in a liquid environment [38, 96].

Our measurement sensitivity could potentially be impacted by various fluctuations in the microfluidic environment that include tumbling of the magnetic particle and temperature fluctuations induce by microwave heating of the fluid. We observe the Zeeman splitting due to the induced field from the magnetic particle in Figure 28. These results rule out the possibility that the magnetic particle is tumbling significantly, and indicate that the applied external magnetic field strongly orients the particle in a fixed direction. A tumbling magnetic particle would make the ESR spectrum broaden, not change the Zeeman splitting [96]. We also calculate the center frequency between the two resonances to be 2.863 MHz in all three cases indicating that we do not observe a heat induced shift due to microwave excitation. A temperature increase would shift

both resonances in the same direction and thus change the ESR center frequency [95, 123, 124], but would not significantly affect the Zeeman splitting.

We note that the contrast of the ESR spectrum is reduced in Figure 28c as compared to Figure 28a. We attribute this reduction in contrast to increased background from scattering of the white light source by the magnetic particle. We observe a photon count rate of 45 kCts/s in Figure 3a which increases to 75 kCts/s in Figure 28c. Since the NV excitation power remains the same in both measurements, the increased count rate results from the particle being brought closer to the spatial position where we collect light and direct it to the photodiode. Although two spots are well resolved on the camera in Figure 28c, we use a pinhole spatial filter on the photodiode that is slightly larger than the diffraction spot in order to reduce the sensitivity of the system to sample drift. As the particle gets closer to the NV center, it therefore scatters more light through the spatial filter resulting in an increased background level. This background could be eliminated in principle by using a stroboscopic measurement approach that switches the white light on to track and then off to measure with the photodiode.

To map out the magnetic field distribution of the magnetic particle, we position it at various horizontal distances r relative to the NV center and measure the variation in Zeeman splitting. We can approximate the spherical magnetic particle as a magnetic dipole when its radius is small compared to the distance r. Figure 29a plots the calculated magnitude of the magnetic field along the glass surface for a magnetic dipole

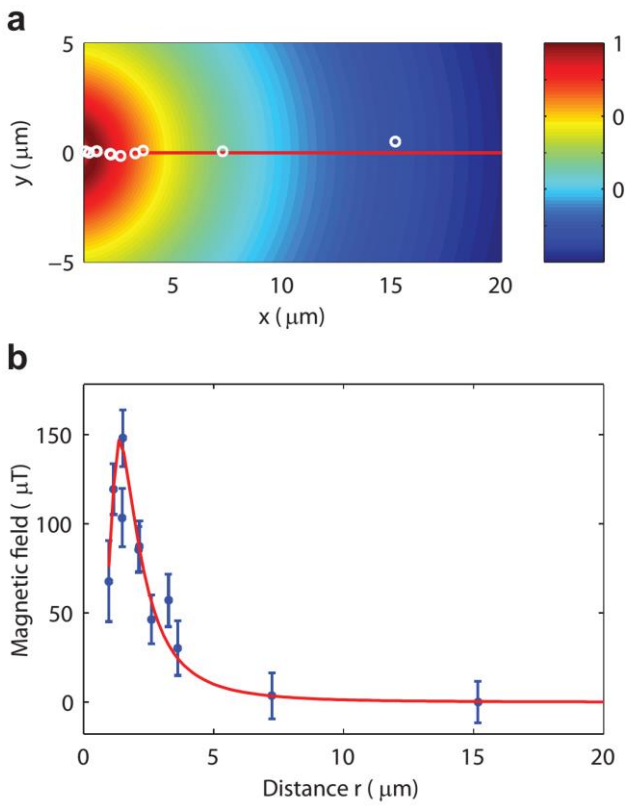

Figure 29: (a) Calculated magnetic field intensity of a magnetic dipole as a function of distance. Open white circles represent experimentally sampled positions of the magnetic field. (b) Measured magnetic field at the various positions represented by the open circles in panel a. Error bars denote the 95% confidence bound of the Lorentzian fit to the ESR spectra. The red curve represents the theoretically calculated magnetic field for the magnetic particle, assumed to be a magnetic dipole.

whose dipole moment points normal to the device surface. The open circles represent positions of the magnetic particle relative to the NV center where we sampled the

magnetic field. Figure 29b plots the measured magnetic fields of the magnetic particle, obtained from the change in Zeeman splitting, as a function of distance *r*. Error bars denote the 95 % confidence bound of the Lorentzian fit used to find the center frequencies of the two Zeeman split ESR transitions. The red curve represents the theoretically predicted magnetic field along the glass surface for a point magnetic dipole. In these calculations, we treat the magnitude of the particle's magnetic moment and orientation of the NV center as fitting parameters. We note that the dipole model is only accurate when the distance of the particle to the NV center exceeds the particle radius (500 nm). This condition is satisfied for virtually all the data points in the figure.

4.5 Summery

In this chapter, we have developed a microfluidic platform to perform NV magnetometry and map localized magnetic fields of magnetic objects. Our method can be extended to scan any particle that we can image and manipulate by flow, making it highly versatile and largely agnostic to the target being scanned. We can improve the magnetic field sensitivity of our system by using NV centers in ultra-pure diamond which have longer coherence times [125, 126], and by utilizing pulsed measurement techniques using Ramsey interferometry that can improve the sensitivity down to $nT/Hz^{1/2}$ [74, 75]. Furthermore, the results reported here using a single NV center can be directly extended to multiple NV centers at different locations of the device surface that serve as parallel sensors for vector magnetometry. They can also be adapted to exploit the electric field [127] and thermal gradient [123, 124] sensing capabilities of NV centers to measure other physical parameters. The presented NV magnetometry system could ultimately lead to highly functional microfluidic systems that combine single particle manipulation and real-time sensing to enable a broad range of applications in the study of biological and chemical systems.

Chapter 5: Nanoscale magnetic field detection using multiple NV centers

5.1 Introduction

We have discussed a method for scanning magnetic field with nanometer spatial resolution in a microfluidic channel. This technique takes advantages of the electron spin resonance of a single NV center and the nanoscale positioning of magnetic nanoparticles using microfluidic flow controls. Using this technique, we are able to map out the magnetic profile of a magnetic nanoparticle. Due to the configuration of an immobilized NV center and a suspended magnetic nanoparticle, however, it is limited to apply this magnetic sensing technique to complex nanostructures and biological samples. Although we control the magnetic dipole direction of the magnetic nanoparticles using external magnetic field, rotational dynamics of the suspended nanoparticles are uncontrollable. In order to image complex magnetic fields, a new scanning method is required.

In this chapter, we introduce a scanning prove technique that employs multiple NV centers in diamond nanocrystals suspended in microfluidic channels. Using microfluidic flow positioning system, we can position diamond nanocrystals in a microfluidic device, simultaneously measuring the external magnetic fields via electron spin resonance transitions of an ensemble of NV centers in the diamond nanocrystals. The multiple NV centers enable to average out the random rotational motion of orientation of NV centers suspended in the fluid, as well as provide a high fluorescence intensity that leads to better signal to noise ratio. We propose a fast magnetic field detection technique employing single frequency ESR measurements. The advantages

of short acquisition time over wide-field with nanoscale resolution make our technique an attractive to a wide range of magnetic imaging applications in fluidic environments and biophysical systems.

5.2 Positioning NV center with flow control

Figure 30 is a schematic of the microfluidic system we have developed to manipulate a diamond nanocrystal and perform localized magnetometry. The device is composed of two microfluidic channels formed between a glass cover slip (1 in x 1 in wide, 150 μm thick) and a molded block of polydimethylsiloxane (PDMS). The microfluidic channels are filled with a viscous fluid that contains target diamond nanocrystals in a liquid suspension. In addition to increasing the fluid viscosity, the fluid also serves to push the diamond nanocrystals to the surfaces of the device [33, 55]. We find that the diamond nanocrystals are preferably confined at the top PDMS surface of the microfluidic channels. We manipulate diamond nanocrystals in the plane of the microfluidic device by applying voltages at the four ends of the microfluidic channels and using feedback control [33, 54, 55]. The voltages induce electroosmotic flow that moves the suspended magnetic particle towards desired directions by viscous drag.

In order to perform optically detected ESR measurements [74], we lithographically pattern a microwave antenna (500 nm Au, 10 nm Ti) on the glass cover slip surface in order to drives the spin transition of the NV center. Figure 31a shows an optical image of the microfluidic device with the integrated microwave antenna. We align the microfluidic channel such that the microwave antenna is as close as possible to the control chamber without directly penetrating into it. A tunable microwave signal generator (ROHDE&SCHWARZ SMC100A) drives the antenna over a spectral range that spans the entire ESR resonance of the NV center (centered at 2.87 GHZ).

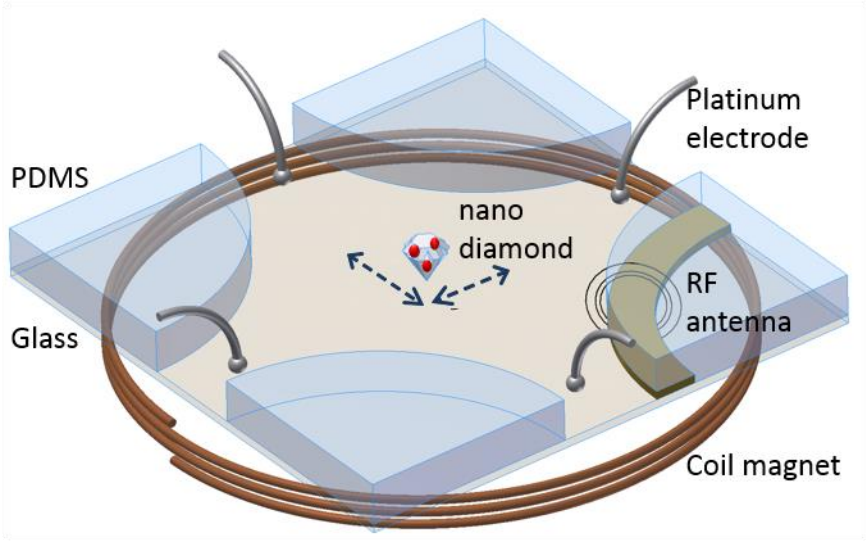

Figure 30: Schematic of microfluidic device used to implement NV magnetometry.

We mount the microfluidic device on a wide-field confocal microscope that excites the sample and collects fluorescence emission from NV ensembles in a diamond nanocrystal through the bottom glass cover slip using a 1.45 numerical aperture oil immersion objective. We excite the NV center using a 532 nm continuous wave laser. The excitation laser beam is widely focused to a 100 μm diameter. The collected light is spectrally filtered using a 600-750 nm bandpass filter to isolate the emission from the NV centers and reject the background signal with a high extinction ratio. The filtered NV emission is projected onto an EM-CCD camera (Hamamatsu C9100-13) to track the diamond nanocrystal and to perform optically detected ESR measurements

using a 20 Hz camera frame rate. In this way, we can measure magnetic fields over a wide-field of view.

Figure 31b shows an EM-CCD camera image of a single diamond nanocrystal in the control chamber of the microfluidic device. We focus on a 21 x 21 pixel area (~2.7 x 2.7 μm2) around the collected emission and then fit diffraction spot to a two dimensional Gaussian point-spread function to determine the centroid position [128]. The cross marker indicates the centroid position of the diamond naocrystal. The special resolution of our tracking algorithm is determined as good as 8 nm in chapter 2.

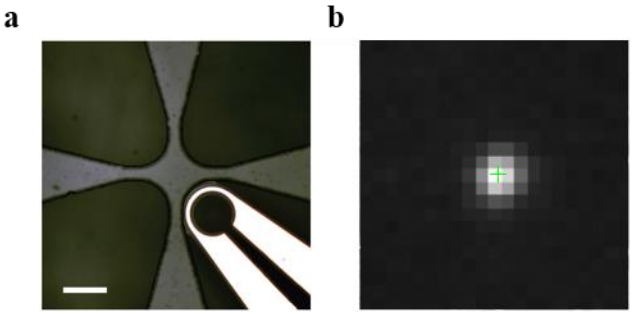

Figure 31: (a) Optical image of the control chamber of the microfluidic device along with integrated microwave antenna. Scale bar is 100 μm. (b) EM-CCD image of a diamond nanocrystal suspended inside the microfluidic control chamber. Green cross marker represents the centroid position of the diamond nanocrystal.

We first investigate the ability to manipulate a diamond nanocrystal within the microfluidic control chamber. Figure 32(a-c) shows a sequence of camera images of a single diamond nanocrystal that we manipulate on the PDMS surface to undergo a predefined trajectory using feedback control. The panels show the position of the diamond nanocrystal at three different times (100, 200, and 300 sec). The magenta boxes current positions of the diamond nanocrystal in the trajectory. The white line shows the past history of the measured positions of the controlled diamond nanocrystal.

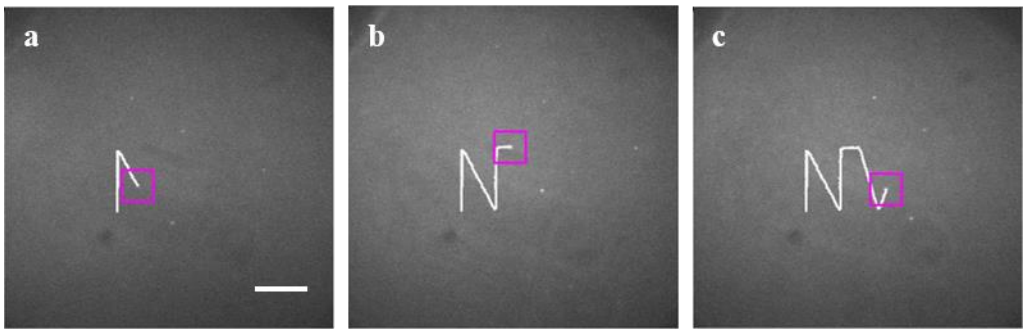

Figure 32: Camera images of a diamond nanocrystal manipulated along a 2D trajectory. The magenta boxes indicate the current location of the diamond nanocrystal at (a) 100 s, (b) 200 s, and (c) 300 s respectively. The white line shows the past history of the measured positions. Scale bar is 10 μm.

In order to determine the positioning accuracy we hold the diamond nanocrystal at a desired location for 3 minutes and continuously monitor its position. Figure 33a shows a two-dimensional plot of the measured positions, and Figure 33b,c show position histograms along x and y direction respectively. We fit each histogram to a Gaussian

(red solid line) and determine a standard deviation of 41 (43) nm along the x (y) directions respectively.

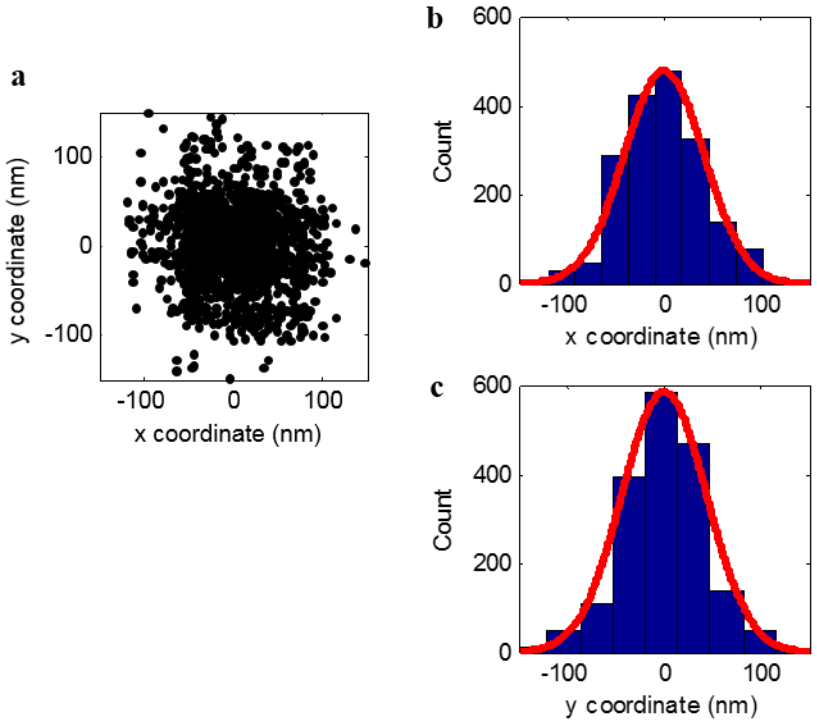

Figure 33: Scatter plots of the measured positions of the diamond nanocrystal held in place using flow control for 3 minutes. (b,c) Position histograms along the x and y axes of panel a. The solid lines are Gaussian fits to the position histograms. The standard deviation is 41 (43) nm along the x (y) directions respectively.

5.3 Multiple NV centers in diamond nanocrystal

The Brownian motion of the suspended diamond nanocrystal randomizes the orientation of NV center to the direction of the excitation laser and the microwave signal. It causes photoluminescence intensity fluctuations of the NV centers in the ESR measurements. To overcome the tumbling effects, we use diamond nanocrystals with mean size of 50 nm that have been engineered to create approximately 25 NV centers in each nanocrystal. In addition to the averaging rotational diffusion motion, the diamond nanocrystal with a high concentration of NV centers also serve as point-like emitter with exceptional brightness. It increases the signal to background noise ratio in the ESR measurements.

We perform the ESR measurements using a software based lock-in approach [96]. This technique eliminates photoluminescence intensity fluctuations that arise from instability of the NV center emission caused by charge fluctuations on the surface [96, 121], and other slow intensity fluctuations induced by the microfluidic environment. We perform lock-in by modulating the microwave power supply on and off at a 10 Hz rate, synchronized with the camera frame rate of 20 Hz, as depicted in Figure 34. We obtain the fluorescence intensity of the NV centers by summing the CCD camera pixels within the tracking region shown in Figure 31b. The two continuous images taken under different microwave excitation contribute a single measurement data point. We define the photoluminescence intensity contrast of the NV centers as

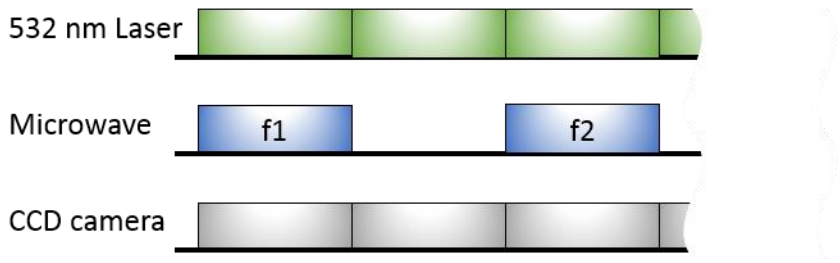

Figure 34: Schematic of software based lock-in. CCD camera is synchronized with microwave signal generator. The microwave power supply is modulated on and off at a 10 Hz rate, synchronized with the camera frame rate of 20 Hz CCD camera exposes. 532 nm laser is constant.

$$C(f) = \frac{I_{on}(f) - I_{off}(f)}{I_{off}(f)}, \tag{4}$$

where I_{on} and I_{off} are the measured photoluminescence intensities with CCD camera images when the microwave is on and off respectively at each value of the microwave frequency.

Figure 00 shows the ESR spectrum of an ensemble of NV centers embedded in a diamond nanocrystal by taking CCD camera images while sweeping the microwave frequency. We observe that the measured ESR spectral peak is broaden due to the averaging over all isotropic NV centers randomly distributed to the fixed optical and

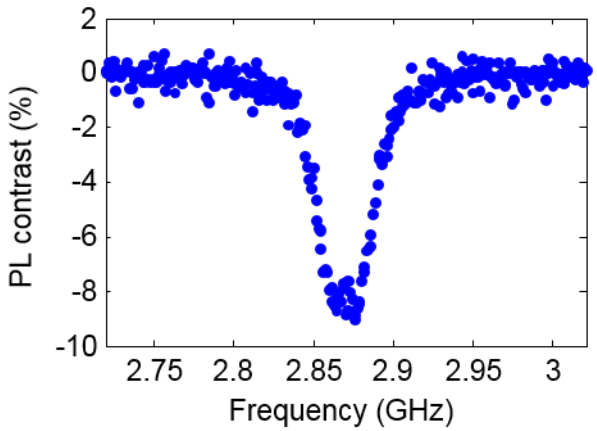

Figure 35: Optically detected ESR spectrum of the ensemble of NV centers.

microwave transition axes. We note that the strain effect in nanocrystal splits the ESR spectra into two peaks, centered at spin resonance frequency of 2.87 GHz.

5.4 Magnetic field detection with CCD camera images

We can optically measure the external magnetic fields by monitoring the ESR spectrum. However, it requires a long measurement time to acquire the full EST spectrum. To reduce total acquisition time, we focus on the PL contrast of the NV centers with a microwave signal fixed at the spin resonance frequency. Specifically, this technique is able to read-out the external magnetic fields using two CCD camera images of the NV centers when the microwave transition is on and off the resonance respectively. This method opens up the possibility of ultra-fast magnetic field imaging applications of tracking dynamics in physical and biological sciences.

To measure the optical response of an ensemble of NV centers to the external magnetic fields, we use a DC coil magnet placed under the microfluidic device. The coil magnet produces a uniform static magnetic field in the direction orthogonal to the PDMS surface of the microfluidic device. Figure 36 shows the PL contrast of the NV centers in a diamond nanocrystal suspended in the microfluidic channels as a function of the voltage driving the coil magnet. We observe that the PL contrast is insensitive to the week magnetic field due to the hyperfine coupling of the NV centers to the nearby ^{14}N nuclear spins, which are introduced for the NV center creation. Once it overcomes the hyperfine coupling, the PL contrast is linearly decreased as the magnetic field increases. The slop of PL contrast curve indicates the magnetic sensitivity of the NV center. We note that the magnetic sensitivity can be improved by using NV centers in

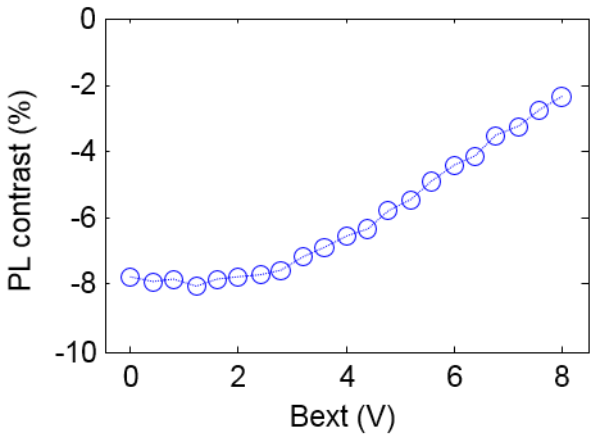

Figure 36: Measured photoluminescence contrast at the various magnetic field intensities.

high purity diamond nanocrystals, which have longer coherence times [125, 126], and by optimizing optical and microwave excitation conditions.

5.5 Summery

In this chapter, we have developed the microfluidic NV magnetometry with ensemble of NV centers in diamond nanocrystals, suspended in the fluid. The deterministic positioning of diamond nanocrystals enables to scan complex nanostructures and biological samples that we can image, making it highly versatile and largely agnostic to the target being scanned. The single frequency ODMR measurement enables monitor dynamics in physical and biological sciences. The CCD camera detection provides wide-field magnetometry with nanoscale spatial resolution. The presented NV magnetometry system could ultimately lead to highly functional microfluidic systems that combine single particle manipulation and real-time sensing to enable a broad range of applications in the study of biological and chemical systems.

Chapter 6: Conclusion and future directions

We demonstrated that nanoparticles can significantly distort the tracking accuracy of a single emitter when performing super-resolution imaging. We observed that the nanoparticle shifts the centroid position of the quantum dot up to 35 nm. Large position displacement occurs even at distance of up to 300 nm from the nanoparticle position. The presence of the nanoparticle causes the position of the emitter to appear pushed away from the surface of the nanoparticle. Our probing approach would enable to study the complex interaction between nanostructures and single emitters as well as optimize nanophotonic systems using single emitter tracking.

Additionally, we demonstrated that the distortion of the emitter's diffraction spot is strongly position dependent to the nanoparticle and the distortion information can be used to reconstruct high-resolution images of the nanoparticle. Using this technique, we achieved fine images of a gold nanosphere with a diameter of 150 nm. Furthermore, we demonstrated a method that can optically track the orientation of a single metal nanorod suspended in the fluid. This method makes possible to extend the distortion based super-resolution imaging technique to non-spherical nanoparticles. In contrast to other super-resolution imaging technique, which require specific surface preparations, our technique is highly flexible to the surface-coating of the nanoparticles and able to provide in-situ imaging of the nanoparticle suspended in microfluidic devices.

We demonstrated a microfluidic platform that can optically detect the localized magnetic fields using a single NV center in am immobilized diamond nanocrystal.

Using this technique, we mapped up magnetic fields distribution of the magnetic nanoparticle manipulated in a microfluidic device with nanometer spatial resolution and high sensitivity. We can improve the magnetic field sensitivity of our system by utilizing pulsed measurement techniques using Ramsey interferometry. The results reported here using a single NV center can be directly extended to multiple NV centers at different locations of the device surface that serve as parallel sensors for vector magnetometry.

We further developed the microfluidic NV magnetometry with ensemble of NV centers in diamond nanocrystals, suspended in the fluid. The deterministic positioning of diamond nanocrystals enables to scan complex nanostructures and biological samples that we can image, making it highly versatile and largely agnostic to the target being scanned. The single frequency ODMR measurement enables monitor dynamics in physical and biological sciences. The CCD camera detection provides wide-field magnetometry with nanoscale spatial resolution. The presented NV magnetometry system could ultimately lead to highly functional microfluidic systems that combine single particle manipulation and real-time sensing to enable a broad range of applications in the study of biological and chemical systems.

Bibliography

1. Huang X, El-Sayed IH, Qian W, El-Sayed MA. Cancer Cell Imaging and Photothermal Therapy in the Near-Infrared Region by Using Gold Nanorods. *Journal of the American Chemical Society* 2006; 128:2115-2120

2. Ando J, Fujita K, Smith NI, Kawata S. Dynamic SERS Imaging of Cellular Transport Pathways with Endocytosed Gold Nanoparticles. *Nano Letters* 2011; 11:5344-5348

3. Gu Y, Sun W, Wang G, Fang N. Single Particle Orientation and Rotation Tracking Discloses Distinctive Rotational Dynamics of Drug Delivery Vectors on Live Cell Membranes. *Journal of the American Chemical Society* 2011; 133:5720-5723

4. Christopher P, Xin H, Linic S. Visible-light-enhanced catalytic oxidation reactions on plasmonic silver nanostructures. *Nat Chem* 2011; 3:467-472

5. Zhou X, Andoy NM, Liu G, et al. Quantitative super-resolution imaging uncovers reactivity patterns on single nanocatalysts. *Nat Nano* 2012; 7:237-241

6. Hao E, Schatz GC. Electromagnetic fields around silver nanoparticles and dimers. *The Journal of Chemical Physics* 2004; 120:357-366

7. Halas NJ, Lal S, Chang W-S, Link S, Nordlander P. Plasmons in Strongly Coupled Metallic Nanostructures. *Chemical Reviews* 2011; 111:3913-3961

8. Michaels AM, Jiang, Brus L. Ag Nanocrystal Junctions as the Site for Surface-Enhanced Raman Scattering of Single Rhodamine 6G Molecules. *The Journal of Physical Chemistry B* 2000; 104:11965-11971

9. Arruebo M, Fernández-Pacheco R, Ibarra MR, Santamaría J. Magnetic nanoparticles for drug delivery. *Nano Today* 2007; 2:22-32

10. Sun C, Lee JSH, Zhang M. Magnetic nanoparticles in MR imaging and drug delivery. *Advanced Drug Delivery Reviews* 2008; 60:1252-1265

11. Lewin M, Carlesso N, Tung C-H, et al. Tat peptide-derivatized magnetic nanoparticles allow in vivo tracking and recovery of progenitor cells. *Nat Biotech* 2000; 18:410-414

12. Pamme N, Wilhelm C. Continuous sorting of magnetic cells via on-chip free-flow magnetophoresis. *Lab on a Chip* 2006; 6:974-980

13. Fang C, Zhang M. Multifunctional magnetic nanoparticles for medical imaging applications. *Journal of Materials Chemistry* 2009; 19:6258-6266

14. Abbe E. Beiträge zur Theorie des Mikroskops und der mikroskopischen Wahrnehmung. *Archiv für mikroskopische Anatomie* 1873; 9:413-418

15. Yildiz A, Forkey JN, McKinney SA, Ha T, Goldman YE, Selvin PR. Myosin V Walks Hand-Over-Hand: Single Fluorophore Imaging with 1.5-nm Localization. *Science* 2003; 300:2061-2065

16. Qu X, Wu D, Mets L, Scherer NF. Nanometer-localized multiple single-molecule fluorescence microscopy. *Proceedings of the National Academy of Sciences of the United States of America* 2004; 101:11298-11303

17. Gordon MP, Ha T, Selvin PR. Single-molecule high-resolution imaging with photobleaching. *Proceedings of the National Academy of Sciences of the United States of America* 2004; 101:6462-6465

18. Rust MJ, Bates M, Zhuang X. Sub-diffraction-limit imaging by stochastic optical reconstruction microscopy (STORM). *Nat Meth* 2006; 3:793-796

19. Manley S, Gillette JM, Patterson GH, et al. High-density mapping of single-molecule trajectories with photoactivated localization microscopy. *Nat Meth* 2008; 5:155-157

20. Mortensen KI, Churchman LS, Spudich JA, Flyvbjerg H. Optimized localization analysis for single-molecule tracking and super-resolution microscopy. *Nat Meth* 2010; 7:377-381

21. Thompson RE, Larson DR, Webb WW. Precise Nanometer Localization Analysis for Individual Fluorescent Probes. *Biophysical Journal* 2002; 82:2775-2783

22. Willets KA, Stranahan SM, Weber ML. Shedding Light on Surface-Enhanced Raman Scattering Hot Spots through Single-Molecule Super-Resolution Imaging. *The Journal of Physical Chemistry Letters* 2012; 3:1286-1294

23. Betzig E, Patterson GH, Sougrat R, et al. Imaging Intracellular Fluorescent Proteins at Nanometer Resolution. *Science* 2006; 313:1642-1645

24. Lakadamyali M, Babcock H, Bates M, Zhuang X, Lichtman J. 3D Multicolor Super-Resolution Imaging Offers Improved Accuracy in Neuron Tracing. *PLoS ONE* 2012; 7:e30826

25. Jones SA, Shim S-H, He J, Zhuang X. Fast, three-dimensional super-resolution imaging of live cells. *Nat Meth* 2011; 8:499-505

26. Huang B, Jones SA, Brandenburg B, Zhuang X. Whole-cell 3D STORM reveals interactions between cellular structures with nanometer-scale resolution. *Nat Meth* 2008; 5:1047-1052

27. Roeffaers MBJ, Sels BF, Uji-i H, et al. Spatially resolved observation of crystal-face-dependent catalysis by single turnover counting. *Nature* 2006; 439:572-575

28. Xu W, Shen H, Kim YJ, et al. Single-Molecule Electrocatalysis by Single-Walled Carbon Nanotubes. *Nano Letters* 2009; 9:3968-3973

29. Chen P, Zhou X, Andoy NM, et al. Spatiotemporal catalytic dynamics within single nanocatalysts revealed by single-molecule microscopy. *Chemical Society Reviews* 2014; 43:1107-1117

30. Stranahan SM, Willets KA. Super-resolution Optical Imaging of Single-Molecule SERS Hot Spots. *Nano Letters* 2010; 10:3777-3784

31. Cang H, Labno A, Lu C, et al. Probing the electromagnetic field of a 15-nanometre hotspot by single molecule imaging. *Nature* 2011; 469:385-388

32. Blythe KL, Mayer KM, Weber ML, Willets KA. Ground state depletion microscopy for imaging interactions between gold nanowires and fluorophore-labeled ligands. *Physical Chemistry Chemical Physics* 2013; 15:4136-4145

33. Ropp C, Cummins Z, Nah S, Fourkas JT, Shapiro B, Waks E. Nanoscale imaging and spontaneous emission control with a single nano-positioned quantum dot. *Nat Commun* 2013; 4:1447

34. Andoy NM, Zhou X, Choudhary E, Shen H, Liu G, Chen P. Single-Molecule Catalysis Mapping Quantifies Site-Specific Activity and Uncovers Radial Activity Gradient on Single 2D Nanocrystals. *Journal of the American Chemical Society* 2013; 135:1845-1852

35. Xiao L, Wei L, He Y, Yeung ES. Single Molecule Biosensing Using Color Coded Plasmon Resonant Metal Nanoparticles. *Analytical Chemistry* 2010; 82:6308-6314

36. Taminiau TH, Stefani FD, Segerink FB, van Hulst NF. Optical antennas direct single-molecule emission. *Nat Photon* 2008; 2:234-237

37. Moerland RJ, Taminiau TH, Novotny L, van Hulst NF, Kuipers L. Reversible Polarization Control of Single Photon Emission. *Nano Letters* 2008; 8:606-610

38. Geiselmann M, Juan ML, Renger J, et al. Three-dimensional optical manipulation of a single electron spin. *Nat Nano* 2013; 8:175-179

39. García NSLaJMaR. Large area nanoscale patterning of silicon surfaces by parallel local oxidation. *Nanotechnology* 2009; 20:475304

40. Sung H, Lee J, Han K, et al. Controlled positioning of metal nanoparticles in an organic light-emitting device for enhanced quantum efficiency. *Organic Electronics* 2014; 15:491-499

41. Huck A, Kumar S, Shakoor A, Andersen UL. Controlled Coupling of a Single Nitrogen-Vacancy Center to a Silver Nanowire. *Physical Review Letters* 2011; 106:096801

42. Geiselmann M, Marty R, Renger J, García de Abajo FJ, Quidant R. Deterministic Optical-Near-Field-Assisted Positioning of Nitrogen-Vacancy Centers. *Nano Letters* 2014; 14:1520-1525

43. Kayci M, Chang H-C, Radenovic A. Electron Spin Resonance of Nitrogen-Vacancy Defects Embedded in Single Nanodiamonds in an ABEL Trap. *Nano Letters* 2014; 14:5335-5341

44. Tetienne JP, Hingant T, Kim JV, et al. Nanoscale imaging and control of domain-wall hopping with a nitrogen-vacancy center microscope. *Science* 2014; 344:1366-1369

45. Braun G, Diechtierow M, Wilkinson S, et al. Enzyme-Directed Positioning of Nanoparticles on Large DNA Templates. *Bioconjugate Chemistry* 2008; 19:476-479

46. Benson O. Assembly of hybrid photonic architectures from nanophotonic constituents. *Nature* 2011; 480:193-199

47. Sitti M, Hashimoto H. Controlled pushing of nanoparticles: modeling and experiments. *Mechatronics, IEEE/ASME Transactions on* 2000; 5:199-211

48. Chey SJ, Huang L, Weaver JH. Manipulation and writing with Ag nanocrystals on Si(111)-7×7. *Applied Physics Letters* 1998; 72:2698-2700

49. Jauffred L, Richardson AC, Oddershede LB. Three-Dimensional Optical Control of Individual Quantum Dots. *Nano Letters* 2008; 8:3376-3380

50. Ashkin A, Dziedzic JM, Bjorkholm JE, Chu S. Observation of a single-beam gradient force optical trap for dielectric particles. *Optics Letters* 1986; 11:288-290

51. Dienerowitz M, Mazilu M, Dholakia K. Optical manipulation of nanoparticles: a review. *Journal of Nanophotonics* 2008; 2:021875-021875-021832

52. Neuman KC, Chadd EH, Liou GF, Bergman K, Block SM. Characterization of Photodamage to Escherichia coli in Optical Traps. *Biophysical Journal* 1999; 77:2856-2863

53. Probstein RF. *Physicochemical Hydrodynamics: An Introduction*, 2005

54. Ropp C, Probst R, Cummins Z, et al. Manipulating Quantum Dots to Nanometer Precision by Control of Flow. *Nano Letters* 2010; 10:2525-2530

55. Ropp C, Cummins Z, Probst R, et al. Positioning and Immobilization of Individual Quantum Dots with Nanoscale Precision. *Nano Letters* 2010; 10:4673-4679

56. Armani M, Chaudhary S, Probst R, Shapiro B. Using feedback control and micro-fluidics to steer individual particles. In: *Micro Electro Mechanical*

Systems, 2005 MEMS 2005 18th IEEE International Conference on, 2005:855-858

57. Armani MD, Chaudhary SV, Probst R, Shapiro B. Using feedback control of microflows to independently steer multiple particles. *Microelectromechanical Systems, Journal of* 2006; 15:945-956

58. Achard J, Tallaire A, Sussmann R, Silva F, Gicquel A. The control of growth parameters in the synthesis of high-quality single crystalline diamond by CVD. *Journal of Crystal Growth* 2005; 284:396-405

59. Li Hong-Dong and Zou Guang-Tian and Wang Qi-Liang and Cheng Shao-Heng and Li Bo and Lü Jian-Nan and Lü Xian-Yi and Jin Z-S. High-Rate Growth and Nitrogen Distribution in Homoepitaxial Chemical Vapour Deposited Single-crystal Diamond. *Chinese Physics Letters* 2008; 25:1803

60. Liang Q, Yan C-s, Meng Y, et al. Recent advances in high-growth rate single-crystal CVD diamond. *Diamond and Related Materials* 2009; 18:698-703

61. Ohno K, Joseph Heremans F, de las Casas CF, et al. Three-dimensional localization of spins in diamond using 12C implantation. *Applied Physics Letters* 2014; 105:052406

62. Rabeau JR, Reichart P, Tamanyan G, et al. Implantation of labelled single nitrogen vacancy centers in diamond using N15. *Applied Physics Letters* 2006; 88:023113

63. Pezzagna S, Rogalla D, Becker HW, et al. Creation of colour centres in diamond by collimated ion-implantation through nano-channels in mica. *physica status solidi (a)* 2011; 208:2017-2022

64. Edmonds AM, D'Haenens-Johansson UFS, Cruddace RJ, et al. Production of oriented nitrogen-vacancy color centers in synthetic diamond. *Physical Review B* 2012; 86:035201

65. Mita Y. Change of absorption spectra in type-I \textit{b} diamond with heavy neutron irradiation. *Physical Review B* 1996; 53:11360-11364

66. Orwa JO, Santori C, Fu KMC, et al. Engineering of nitrogen-vacancy color centers in high purity diamond by ion implantation and annealing. *Journal of Applied Physics* 2011; 109:083530

67. Kurtsiefer C, Mayer S, Zarda P, Weinfurter H. Stable Solid-State Source of Single Photons. *Physical Review Letters* 2000; 85:290-293

68. Beveratos A, Brouri R, Gacoin T, Villing A, Poizat J-P, Grangier P. Single Photon Quantum Cryptography. *Physical Review Letters* 2002; 89:187901

69. Jelezko F, Gaebel T, Popa I, Gruber A, Wrachtrup J. Observation of Coherent Oscillations in a Single Electron Spin. *Physical Review Letters* 2004; 92:076401

70. Balasubramanian G, Neumann P, Twitchen D, et al. Ultralong spin coherence time in isotopically engineered diamond. *Nat Mater* 2009; 8:383-387

71. Gruber A, Dräbenstedt A, Tietz C, Fleury L, Wrachtrup J, Borczyskowski Cv. Scanning Confocal Optical Microscopy and Magnetic Resonance on Single Defect Centers. *Science* 1997; 276:2012-2014

72. Manson NB, Harrison JP, Sellars MJ. Nitrogen-vacancy center in diamond: Model of the electronic structure and associated dynamics. *Physical Review B* 2006; 74:104303

73. Degen CL. Scanning magnetic field microscope with a diamond single-spin sensor. *Applied Physics Letters* 2008; 92:-

74. Taylor JM, Cappellaro P, Childress L, et al. High-sensitivity diamond magnetometer with nanoscale resolution. *Nat Phys* 2008; 4:810-816

75. Maze JR, Stanwix PL, Hodges JS, et al. Nanoscale magnetic sensing with an individual electronic spin in diamond. *Nature* 2008; 455:644-647

76. Balasubramanian G, Chan IY, Kolesov R, et al. Nanoscale imaging magnetometry with diamond spins under ambient conditions. *Nature* 2008; 455:648-651

77. Maertz BJ, Wijnheijmer AP, Fuchs GD, Nowakowski ME, Awschalom DD. Vector magnetic field microscopy using nitrogen vacancy centers in diamond. *Applied Physics Letters* 2010; 96:-

78. Schoenfeld RS, Harneit W. Real Time Magnetic Field Sensing and Imaging Using a Single Spin in Diamond. *Physical Review Letters* 2011; 106:030802

79. Gaster RS, Xu L, Han S-J, et al. Quantification of protein interactions and solution transport using high-density GMR sensor arrays. *Nat Nano* 2011; 6:314-320

80. Li G, Joshi V, White RL, et al. Detection of single micron-sized magnetic bead and magnetic nanoparticles using spin valve sensors for biological applications. *Journal of Applied Physics* 2003; 93:7557-7559

81. Dolabdjian C, Qasimi A, Bloyet D, Mosser V. Spatial resolution of SQUID magnetometers and comparison with low noise room temperature magnetic sensors. *Physica C: Superconductivity* 2002; 368:80-84

82. Arcizet O, Jacques V, Siria A, Poncharal P, Vincent P, Seidelin S. A single nitrogen-vacancy defect coupled to a nanomechanical oscillator. *Nat Phys* 2011; 7:879-883

83. MaletinskyP, HongS, Grinolds MS, et al. A robust scanning diamond sensor for nanoscale imaging with single nitrogen-vacancy centres. *Nat Nano* 2012; 7:320-324

84. Rondin L, Tetienne J-P, Spinicelli P, et al. Nanoscale magnetic field mapping with a single spin scanning probe magnetometer. *Applied Physics Letters* 2012; 100:-

85. S Prawer and P Mulvaney and F Jelezko and J Wrachtrup and R E Scholten and L C L Hollenberg LPMaLTHaASaDASaCDHaJHCaKGaBCGa. Ambient nanoscale sensing with single spins using quantum decoherence. *New Journal of Physics* 2013; 15:073042

86. Ermakova A, Pramanik G, Cai JM, et al. Detection of a Few Metallo-Protein Molecules Using Color Centers in Nanodiamonds. *Nano Letters* 2013; 13:3305-3309

87. Kaufmann S, Simpson DA, Hall LT, et al. Detection of atomic spin labels in a lipid bilayer using a single-spin nanodiamond probe. *Proceedings of the National Academy of Sciences* 2013; 110:10894-10898

88. Grinolds MS, Hong S, Maletinsky P, et al. Nanoscale magnetic imaging of a single electron spin under ambient conditions. *Nat Phys* 2013; 9:215-219

89. Rondin L, Tetienne JP, Rohart S, et al. Stray-field imaging of magnetic vortices with a single diamond spin. *Nat Commun* 2013; 4

90. Fu C-C, Lee H-Y, Chen K, et al. Characterization and application of single fluorescent nanodiamonds as cellular biomarkers. *Proceedings of the National Academy of Sciences* 2007; 104:727-732

91. Liu K-K, Cheng C-L, Chang C-C, Chao J-I. Biocompatible and detectable carboxylated nanodiamond on human cell. *Nanotechnology* 2007; 18:325102-325102

92. McGuinness LP, YanY, StaceyA, et al. Quantum measurement and orientation tracking of fluorescent nanodiamonds inside living cells. *Nat Nano* 2011; 6:358-363

93. Le Sage D, Arai K, Glenn DR, et al. Optical magnetic imaging of living cells. *Nature* 2013; 496:486-489

94. Hall LT, Beart GCG, Thomas EA, et al. High spatial and temporal resolution wide-field imaging of neuron activity using quantum NV-diamond. *Sci Rep* 2012; 2

95. Kucsko G, Maurer PC, Yao NY, et al. Nanometre-scale thermometry in a living cell. *Nature* 2013; 500:54-58

96. Horowitz VR, Alemán BJ, Christle DJ, Cleland AN, Awschalom DD. Electron spin resonance of nitrogen-vacancy centers in optically trapped nanodiamonds. *Proceedings of the National Academy of Sciences* 2012; 109:13493-13497

97. Lin H, Centeno SP, Su L, et al. Mapping of Surface-Enhanced Fluorescence on Metal Nanoparticles using Super-Resolution Photoactivation Localization Microscopy. *ChemPhysChem* 2012; 13:973-981

98. Willets KA. Super-resolution imaging of interactions between molecules and plasmonic nanostructures. *Physical Chemistry Chemical Physics* 2013; 15:5345-5354

99. Ropp C, Cummins Z, Nah S, Fourkas JT, Shapiro B, Waks E. Nanoscale probing of image-dipole interactions in a metallic nanostructure. *Nat Commun* 2015; 6

100. Ober RJ, Ram S, Ward ES. Localization Accuracy in Single-Molecule Microscopy. *Biophysical Journal*; 86:1185-1200

101. Donehue JE, Wertz E, Talicska CN, Biteen JS. Plasmon-Enhanced Brightness and Photostability from Single Fluorescent Proteins Coupled to Gold Nanorods. *The Journal of Physical Chemistry C* 2014; 118:15027-15035

102. Wertz E, Isaacoff BP, Flynn JD, Biteen JS. Single-Molecule Super-Resolution Microscopy Reveals How Light Couples to a Plasmonic Nanoantenna on the Nanometer Scale. *Nano Letters* 2015; 15:2662-2670

103. Lim K, Ropp C, Shapiro B, Taylor JM, Waks E. Scanning Localized Magnetic Fields in a Microfluidic Device with a Single Nitrogen Vacancy Center. *Nano Letters* 2015; 15:1481-1486

104. Shimizu KT, Neuhauser RG, Leatherdale CA, Empedocles SA, Woo WK, Bawendi MG. Blinking statistics in single semiconductor nanocrystal quantum dots. *Physical Review B* 2001; 63:205316

105. Mulvaney P. Materials Mix. Optical properties of metal clusters By U. Kreibig, M. Vollmer, Springer Series in Materials Science, Vol. 25, Springer, Berlin 1995, XVII, 532 pp., Hardcover, DM 98.00, ISBN 3-540-57836-6. *Advanced Materials* 1996; 8:699-699

106. Moore T. ABSORPTION AND SCATTERING OF LIGHT BY SMALL PARTICLES by C.F. Bohren and D.R. Huffman, Wiley Science Paperback Series, Chichester, UK, 1998, xiv+530 pp., List of references, index (£34.95; pbk). *Robotica* 1998; 16:703-703

107. Zijlstra P, Chon JWM, Gu M. Five-dimensional optical recording mediated by surface plasmons in gold nanorods. *Nature* 2009; 459:410-413

108. Schubert O, Becker J, Carbone L, et al. Mapping the Polarization Pattern of Plasmon Modes Reveals Nanoparticle Symmetry. *Nano Letters* 2008; 8:2345-2350

109. Kelly KL, Coronado E, Zhao LL, Schatz GC. The Optical Properties of Metal Nanoparticles: The Influence of Size, Shape, and Dielectric Environment. *The Journal of Physical Chemistry B* 2003; 107:668-677

110. Chen H, Shao L, Li Q, Wang J. Gold nanorods and their plasmonic properties. *Chemical Society Reviews* 2013; 42:2679-2724

111. Ming T, Zhao L, Yang Z, et al. Strong Polarization Dependence of Plasmon-Enhanced Fluorescence on Single Gold Nanorods. *Nano Letters* 2009; 9:3896-3903

112. Yi C, Li C-W, Ji S, Yang M. Microfluidics technology for manipulation and analysis of biological cells. *Analytica Chimica Acta* 2006; 560:1-23

113. Hoyoung Yun and Kisoo Kim and Won Gu L. Cell manipulation in microfluidics. *Biofabrication* 2013; 5:022001

114. Steinert S, Ziem F, Hall LT, et al. Magnetic spin imaging under ambient conditions with sub-cellular resolution. *Nat Commun* 2013; 4:1607

115. Micheal A, Satej C, Roland P, Shawn W, Benjamin S. Control of microfluidic systems: two examples, results, and challenges. *International Journal of Robust and Nonlinear Control* 2005; 15:785-803

116. Cohen AE. Control of Nanoparticles with Arbitrary Two-Dimensional Force Fields. *Physical Review Letters* 2005; 94:118102

117. Chaudhary S, Shapiro B. Arbitrary steering of multiple particles independently in an electro-osmotically driven microfluidic system. *Control Systems Technology, IEEE Transactions on* 2006; 14:669-680

118. Komaee A, Shapiro B. Steering a Ferromagnetic Particle by Optimal Magnetic Feedback Control. *Control Systems Technology, IEEE Transactions on* 2012; 20:1011-1024

119. Nacev A, Komaee A, Sarwar A, et al. Towards Control of Magnetic Fluids in Patients: Directing Therapeutic Nanoparticles to Disease Locations. *Control Systems, IEEE* 2012; 32:32-74

120. Zhaolong S, Chen K, Shapiro B. Measuring low concentrations of fluorescent magnetic nanoparticles by fluorescence microscopy. In: *Manipulation, Manufacturing and Measurement on the Nanoscale (3M-NANO), 2012 International Conference on*, 2012:283-287

121. BradacC, GaebelT, NaidooN, et al. Observation and control of blinking nitrogen-vacancy centres in discrete nanodiamonds. *Nat Nano* 2010; 5:345-349

122. Dréau A, Lesik M, Rondin L, et al. Avoiding power broadening in optically detected magnetic resonance of single NV defects for enhanced dc magnetic field sensitivity. *Physical Review B* 2011; 84:195204

123. Toyli DM, Christle DJ, Alkauskas A, Buckley BB, Van de Walle CG, Awschalom DD. Measurement and Control of Single Nitrogen-Vacancy Center Spins above 600 K. *Physical Review X* 2012; 2:031001

124. Toyli DM, de las Casas CF, Christle DJ, Dobrovitski VV, Awschalom DD. Fluorescence thermometry enhanced by the quantum coherence of single spins in diamond. *Proceedings of the National Academy of Sciences* 2013; 110:8417-8421

125. Ishikawa T, Fu K-MC, Santori C, et al. Optical and Spin Coherence Properties of Nitrogen-Vacancy Centers Placed in a 100 nm Thick Isotopically Purified Diamond Layer. *Nano Letters* 2012; 12:2083-2087

126. Huang Z, Li W-D, Santori C, et al. Diamond nitrogen-vacancy centers created by scanning focused helium ion beam and annealing. *Applied Physics Letters* 2013; 103:-

127. Dolde F, Fedder H, Doherty MW, et al. Electric-field sensing using single diamond spins. *Nat Phys* 2011; 7:459-463

128. Rittweger E, Han KY, Irvine SE, Eggeling C, Hell SW. STED microscopy reveals crystal colour centres with nanometric resolution. *Nat Photon* 2009; 3:144-147